An Atypical Shallow Mw 5.3, 2021 Earthquake in the Western Corinth Rift (Greece)

Jiří Zahradník, El Madani Aissaoui, Pascal Bernard, Pierre Briole, Simon Bufféral, Louis de Barros, Anne Deschamps, Panagiotis Elias, Christos Evangelidis, Ioannis Fountoulakis, et al.

JGR Solid Earth

RESEARCH ARTICLE
10.1029/2022JB024221

An Atypical Shallow Mw 5.3, 2021 Earthquake in the Western Corinth Rift (Greece)

Jiří Zahradník[1], El Madani Aissaoui[2], Pascal Bernard[2], Pierre Briole[3], Simon Bufféral[3], Louis De Barros[4], Anne Deschamps[4], Panagiotis Elias[5], Christos P. Evangelidis[6], Ioannis Fountoulakis[6], František Gallovič[1], Vasilis Kapetanidis[7], George Kaviris[7], Olga-Joan Ktenidou[6], Sophie Lambotte[8], Olivier Lengliné[8], Helene Lyon-Caen[3], Mark Noble[9], Vladimír Plicka[1], Alexis Rigo[3], Zafeiria Roumelioti[10], Anna Serpetsidaki[10], Efthimios Sokos[10], and Nicholas Voulgaris[7]

[1]Faculty of Mathematics and Physics, Charles University, Prague, Czech Republic, [2]Équipe de Sismologie, Institut de Physique du Globe de Paris, Paris, France, [3]Laboratoire de Géologie, CNRS, École Normale Supérieure, PSL University, Paris, France, [4]Université Côte d'Azur, CNRS, Observatoire de la Côte d'Azur, IRD, Géoazur, Nice, France, [5]National Observatory of Athens, Institute for Astronomy, Astrophysics, Space Applications and Remote Sensing, Athens, Greece, [6]National Observatory of Athens, Institute of Geodynamics, Athens, Greece, [7]Section of Geophysics–Geothermics, Department of Geology and Geoenvironment, National and Kapodistrian University of Athens, Athens, Greece, [8]EOST, ITES, Université de Strasbourg, CNRS, Strasbourg, France, [9]Centre de Géosciences, MINES ParisTech, PSL University, Fontainebleau, France, [10]Department of Geology, University of Patras, Patras, Greece

Key Points:

- Seismic, geodetic and tide gauge records in Corinth rift reveal a rare shallow rupture (~0–5 km) on a south-dipping offshore normal fault
- The shallow rupture was preceded, triggered, and followed by microearthquakes mostly occurring deeper, on the detachment layer
- The causative fault is along-dip segmented and rooted beneath detachment as inherited from fault interactions during the rift evolution

Supporting Information:

Supporting Information may be found in the online version of this article.

Correspondence to:

J. Zahradník,
jiri.zahradnik@mff.cuni.cz

Citation:

Zahradník, J., Aissaoui, E. M., Bernard, P., Briole, P., Bufféral, S., De Barros, L., et al. (2022). An atypical shallow Mw 5.3, 2021 earthquake in the western Corinth rift (Greece). *Journal of Geophysical Research: Solid Earth*, *127*, e2022JB024221. https://doi.org/10.1029/2022JB024221

Received 16 FEB 2022
Accepted 2 SEP 2022

Abstract Moderate-to-large earthquakes in rifts may occur on leading boundary faults or inner antithetic faults. Here we show a rare case of the 2020–2021 seismic sequence in the Corinth rift, that culminated in the shallow rupture of the antithetic fault, neither preceded nor followed by the leading fault rupture. The hypocenter of the largest shock (Mw 5.3 of 17 February 2021) was located at ~8 km depth. However, seismic waveform data, supported by satellite-geodetic and tide gauge measurements, pointed to rupture at shallow depth (~3 km), where no earthquakes were previously observed. We show that the earthquake most probably ruptured two orthogonal, conjugate fault segments: a weak nucleation phase occurred in the microseismically highly active sub-horizontal detachment layer, followed – a few seconds later – by a larger, shallow moment release on a high-angle, south-dipping normal fault. The latter is the Mornos offshore fault, antithetic to the leading, north-dipping Psathopyrgos fault. Our study presents the first instrumental/observational evidence of a very shallow Mw 5+ event in this rift – and one of the few reported worldwide. The depth limit of the main shallow slip patch coincides with the expected crossing of the Mornos fault with the Psathopyrgos fault, stressing the importance of fault segmentation and rooting inherited from the rift history. This unusual shallow slip in a depth range with little background seismicity and few aftershocks needs to be further investigated by dynamic modeling as a possible prototype of hazardous events in rift environments.

Plain Language Summary The Corinth rift is a key tectonic element in the Eastern Mediterranean, separating mainland Greece from the Peloponnese. The rift is highly seismically active, yet geologically complex and not fully understood. Between December 2020 and February 2021, thousands of small earthquakes and two Mw > 5 events occurred there. Microearthquakes migrated in the rift on a subhorizontal detachment layer, separating the brittle and ductile crust. Similar activity has been well known for decades. However, the Mw 5.3 mainshock of February 17 was peculiar. While it nucleated at a depth of ~8 km on the detachment, most of the slip occurred at unusually shallow depths of ~0–5 km. This major rupture segment, well constrained by seismic, geodetic, and tide gauge data, is interpreted here as a rare shallow activation of a south-dipping offshore western continuation of the Trizonia fault system. This continuation is most likely the Mornos fault, lying opposite (antithetic) to the major north-dipping Psathopyrgos fault which outcrops on the southern coast. The present complexity of these structures is a result of the tectonic evolution of the rift during the last 0.4 Myr. The gained knowledge, supplemented by new offshore measurement techniques, will improve seismic and tsunami hazard assessment.

1. Introduction

The crustal extension has a variety of forms depending on the involved lithospheric plates (oceanic and continental rifts, back-arc basins, orogen-collapse zones, distributed extensional faulting in high-topography regions, etc.).

Earthquakes in extensional environments typically occur on normal faults; yet another mechanism is also often encountered, such as strike-slip in transtensional shear zones. In rifts, major earthquakes are generally expected to occur on segments of high-angle bordering faults that control rift evolution (Chéry, 2001; Ebinger et al., 2019). However, during the rift development, the leading role can be transferred to other faults (Cowie et al., 2017; Ford et al., 2016). Thus, the association of earthquakes with specific faults can be challenging, particularly offshore, in the inner gulfs or seas of the rifts. The outstanding question is how various types of deformation (e.g., swarm-like microseismicity on detachments, or earthquake sequences on steep faults) complement each other in the rifts. In this paper, we address this question in one of the most active rifts of Europe – the Corinth rift in the Eastern Mediterranean.

Before discussing the Corinth rift, we briefly review extensional zones in general, e.g., what types of seismicity we may face and where large earthquakes could be generated. Extension in continental non-magmatic rifts takes place in the form of brittle faulting and creep. Aseismic creep operates primarily in the lower crust (Doglioni et al., 2015). A sub-horizontal, low-dip (<30°) transition layer of complex rheology is created between the lower ductile and upper brittle crust, substantially assisted by mantle fluids (Le Pourhiet et al., 2003). This low-dip-angle layer called detachment can host microearthquakes, often in swarms, e.g. in certain parts of the Apennines, Italy (Waldhauser et al., 2021). The amount of extension accommodated by microearthquakes can be significant (e.g., 30% of the geodetically measured extension in Taupo Rift in New Zealand, as shown by Mouslopoulou et al., 2013). The physical nature of microearthquakes can be explained, for example, as Riedel's secondary shear structures in a creeping zone (Lecomte et al., 2012). In metamorphic core complexes, the detachment zones are exhumed, appearing as faults, e.g., the Simav detachment fault in Menderes graben (Oner & Dilek, 2011). Nevertheless, significant earthquakes rupturing low-angle normal faults (LANF) are uncommon and still under debate (Styron & Hetland, 2014). Ide et al. (2011) reported a few LANF Mw > 6 earthquakes near the Pacific subducting plate, possibly caused by stress rotation due to the Mw 9.0 2011 Tohoku earthquake. One segment of the complex Ms 6.9 1980 Irpinia earthquake was also interpreted as LANF (Bernard & Zollo, 1989).

Moderate-to-strong earthquakes, requiring a sufficient fault-rupture length, are usually associated with high-angle normal faults in extensional areas. Interactions among them are common, including joint activation of several synthetic and antithetic faults. A typical example is the 2016 Apennines, Italy seismic sequence, with joint involvement of the Vettore fault and the Norcia Antithetic fault (Figure 1c of Walters et al., 2018); their intersection might have determined the bottom limit of the slipped area at ~6 km depth. The steep faults may have roots in the detachment layer (see Figure 4 of Waldhauser et al., 2021). Long faults in wide grabens can penetrate to the lower crust as in the Tanganyika rift (Craig et al., 2011). In the long term, deep fault roots in creeping shear zones may allow for stress loading of the shallow fault segments (Cowie et al., 2013; Kato et al., 2009). In the short term, rupture can be initiated on a low-angle structure and propagate upwards on a high-angle fault (Braunmillller & Nábělek, 1996). A horizontal rupture propagation along high-angle normal faults can dominate for M6+ earthquakes; an example is the Mw 6.3 Lesvos, Aegean earthquake of 2017 (Kiratzi, 2018), dynamically modeled by Kostka et al. (2022). Fault interactions can also include a simultaneous or sequential rupture of conjugate faults, as observed and theoretically justified for the Mw 6.6 Niigata-ken Chuetsu-Oki earthquake of 2007 (Aochi & Kato, 2010).

Seismicity in shallow crustal layers of some extensional regions is low or absent, and physical reasons for such quiescence are not always precisely known. For example, low seismicity has been documented in the uppermost 5 km of the Marangu basin in the Tanganyika rift (Lavayssière et al., 2019) and the upper 1.5 km in the Taupo rift, New Zealand (Mouslopoulou et al., 2013). On the contrary, aftershocks of recent normal-faulting (non-rift) earthquakes in the Apennines, mentioned above, do not mark any substantial near-surface seismically silent layer, and background seismicity during 2008–2020 in the Irpinia faults area (southern Italy) extended up to the Earth surface (Picozzi et al., 2022). Although the sub-surface aseismic layers can participate in the rift extension, e.g., via inelastic yielding (Kaneko & Fialko, 2011), their transition to brittle deformation is less understood. In general, if a shallow layer operates in the velocity-strengthening mode, it may inhibit rupture nucleation but can support a rupture growth from a nearby, perhaps deeper, velocity-weakening zone (Kaneko et al., 2010). In the present paper, we demonstrate a practical example of how these processes may lead to the occurrence of a shallow moderate earthquake in a previously quiescent upper part of a rift.

1.1. Corinth Rift

The Corinth rift is an outstanding example of an extensional crustal structure in the Aegean region (Eastern Mediterranean). It is an active half-graben with an inner gulf, separating the Peloponnese from mainland Greece. It belongs to one of the most seismically active regions of the country, hosting historical M7 earthquakes and instrumental events up to Mw 6.7 (Makropoulos et al., 2012; Stucchi et al., 2013). According to Grünthal and Wahlström (2012), historical seismicity in the rift included two events of M7, namely in 1402 and 1889. Regarding Mw 6.5–7.0, eleven of them occurred between 1580 and 1887, and two after 1900. The locations of historical events, shown in the inset of Figure 1, are only approximate, and cannot be associated with geologically well-identified faults. For example, the M7 of 1889 was recently reinterpreted as Mw∼6.5, which occurred ∼60 km westward, outside the rift (Albini et al., 2017).

Other than moderate-to-large earthquake sequences, the Corinth rift has a rich microseismic (mostly swarm-like) activity. The microseismicity of the rift has been precisely monitored for the last 20 years. Particularly the western Gulf of Corinth (WGoC) is covered by a dense network of the Corinth Rift Laboratory (CRL; http://crlab.eu). The seismic activity, including more than 200,000 located events, is characterized by frequent earthquake swarms (De Barros et al., 2020; Duverger et al., 2015, 2018; Kapetanidis, 2017; Kapetanidis et al., 2015; Kaviris et al., 2017, 2018; Mesimeri et al., 2016; Pacchiani & Lyon-Caen, 2010). The swarms migrate below the gulf and coastal areas. This seismicity is confined to a sub-horizontal detachment zone at depths of 5–10 km, slightly dipping to the north, and the migration can be explained by pore-pressure diffusion (Bourouis & Cornet, 2009; Lambotte et al., 2014), possibly combined with fluid-flow driven aseismic slip episodes (De Barros et al., 2020). Regarding shallow aseismic slip in the Corinth rift, we have no information apart from a single observation of a short-lived (30 minutes) transient slow-slip event in 2001 (Bernard et al., 2006).

In the WGoc, the surface fault traces could be extrapolated down to some seismic clusters at the detachment (see, e.g., Figure 6.19 of Kapetanidis, 2017, or Figure 5 of Duverger et al., 2018). However, no systematic correlation has been found between the microseismicity and the major high-angle normal faults bounding the rift. The main reason is the absence of seismicity in the topmost 4 km of WGoC; in the long term, the number of events shallower than 4 km is less than 1%. Contrary to the swarm migrations and fluid effects on the detachment, referenced above, this 4-km-deep seismically quiescent layer has remained to date practically uncommented in the existing body of literature. This paper demonstrates its crucial significance.

Only two earthquake sequences within WGoC have so far enabled the investigation of likely causative faults: the most recent destructive earthquake of Mw 6.3 in 1995, which caused 26 fatalities and damaged the city of Aigion (Bernard et al., 1997), and the two major events (Mw 5.3 and 5.2) of the 2010 Efpalio sequence (Kapetanidis & Papadimitriou, 2011; Sokos et al., 2012; see also Figure 5.16 of Kapetanidis, 2017). Their rich aftershock sequences occurred at depths greater than 4 km. The 1995 mainshock (centroid depth 7.5 km) was interpreted as a LANF aligned with the detachment layer (Bernard et al., 1997); the horizontal projection of the fault plane of the 1995 event is shown in Figure 1. The two 2010 earthquakes occurred on the northern coast of the gulf, near the surface trace of the major rift-bounding, south-dipping Marathias fault. With centroid depths of 4.5 and 6.0 km, the events appeared to have slip areas located slightly above the detachment zone. The Marathias fault was most likely not the causative one; association with shorter faults in the region, parallel to Marathias, dipping both to the north and south, were considered possible but such studies were inconclusive (Sokos et al., 2012).

The Psathpyrgos fault (Figure 1), marking the western termination of the rift, is a north-dipping, high-angle normal fault, ∼10 km long, outcropping on the southern coast, which controls the long-term tectonic evolution of the western rift (e.g., Chéry, 2001; Ford et al., 2016; Palyvos et al., 2007). However, none of the instrumentally observed moderate earthquakes in WGoC nor any of the major historical earthquakes of 1748, 1817, 1861, 1888, and 1889, with estimated magnitudes from M5.9 to M6.7, were associated with this fault (Albini et al., 2017).

To summarize, in WGoC we do not observe recent seismic activity on shallow parts of the major rift-bounding steep normal faults. In this respect, the Corinth rift differs from other extensional regions, e.g. the Apennines, where microseismic activity on detachments coexists with the recently active high-angle normal faults, as discussed in the preceding section. Most of the (abundant) activity of the last 20 years in WGoC is related to the subhorizontal detachment zone at depths of ∼5–10 km. The depths of 0–4 km appeared quiescent until the most recent reactivation of the western rift, in 2020–2021, for which preliminary results (Kaviris et al., 2021) indicated a possible rupture of the largest event of the sequence (Mw 5.3) at a very shallow depth, < 4 km. The

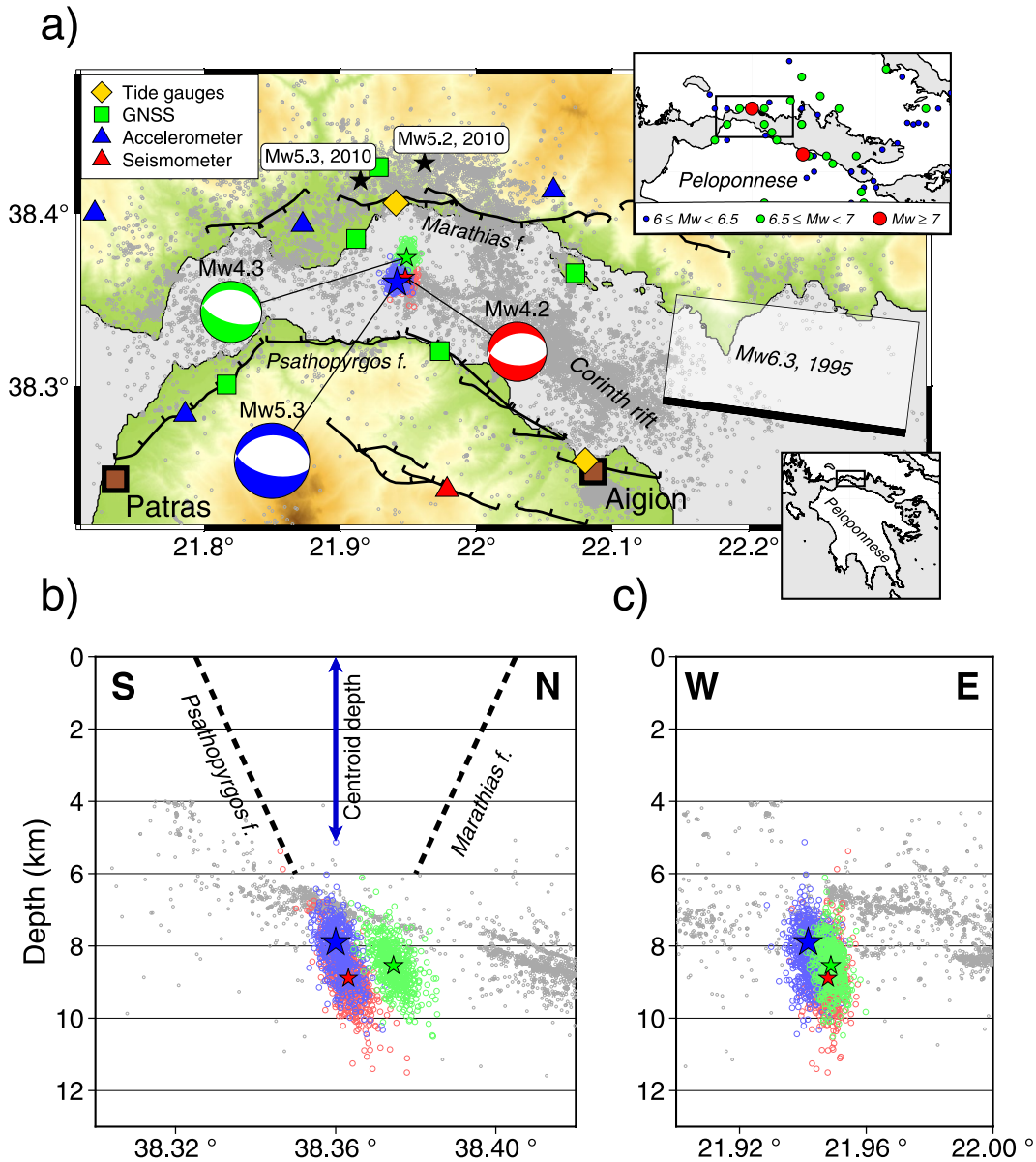

Figure 1. The 17 February 2021 earthquakes in the western Corinth gulf. (a) Hypocenters of the mainshock (Mw 5.3, blue), foreshock (Mw 4.2, red), and aftershock (Mw 4.3, green) are shown with stars, their uncertainty with samples of the probability density function (the colored 'clouds'), focal mechanisms by beachballs. Near seismic, GNSS, and tide gauge stations are also shown (see legend). The epicenters of the 2010 Efpalio events (Mw 5.3 and 5.2, the blacks stars) and the fault plane of the 1995 Aigion earthquake (Mw 6.3, the bold edge is the fault top) are included. Numerous small gray circles depict the previous microseismic activity of 2000–2015 (Duverger et al., 2018), mapping the detachment layer. Faults after Boiselet (2014). Upper inset: Historic seismicity after Grünthal and Wahlström (2012); the catalog starts at 1000 CE. Lower inset: Broader area. (b) and (c) Vertical cross-sections passing through the mainshock hypocenter (projection of microearthquakes ± 4 km off profile). Uncertainty of centroid position is indicated by double-arrow in panel (b).

existence and characteristics of seismogenic structures at these shallow depths however remain unclear, which demands in-depth multidisciplinary study. The goal of this study is to demonstrate a rare case of a moderate earthquake in a long-term quiescent zone, located above the detachment. The observations can hopefully attract the attention of experts in dynamic source modeling, thus yielding in the future a better understanding of this rare phenomenon. Furthermore, this study may improve the understanding of seismic hazards in extension tectonic areas.

1.2. The Mw 5.3 Event of the 2020–2021 Seismic Crisis

Seismic activity at depths ∼5–10 km in the western Corinth rift increased in 2020–2021. The spatiotemporal behavior was analyzed by Kaviris et al. (2021) and Mesimeri et al. (2022). The crisis, involving thousands of events, evolved in the form of three spatial groups and temporal stages, migrating through the WGoC. The groups, defined in Kaviris et al. (2021), are shown in Figure S1 in the Supporting Information S1. The largest event of Mw 5.3 occurred on 17 February 2021 (hereafter **Feb17**, for short). It was accompanied by only two nearby events of Mw ∼ 4, one foreshock and one aftershock, all occurring within two hours (Figure 1). The earthquakes took place less than 20 km from Patras, the third largest city in Greece. They caused limited damage to the highway and railroad connecting the cities of Patras and Aigion, due to ground subsidence on the hanging wall of the Psathopyrgos fault. Thus, fundamental questions arise as to whether the Mw 5.3 earthquake of Feb17 ruptured part of the nearby Psathopyrgos fault, or was rather related to other structures, e.g. antithetic, south-dipping faults in the Gulf, like the Marathias or Trizonia fault systems, shown in Figures 1 and 2 (Beckers et al., 2015; Bell et al., 2008, 2009; Lambotte et al., 2014; Moretti et al., 2003; Palyvos et al., 2005). Such questions are of major importance for seismotectonic and seismic hazard studies, given that the Psathopyrgos fault is in its late interseismic phase, as determined by Boiselet (2014).

As indicated by Kaviris et al. (2021), although the hypocenter was located at a depth of ∼8 km, on the detachment, both the Global Navigation Satellite System (GNSS) data and the seismic data (i.e., centroid position) pointed to a major slip occurring at a shallower depth of <4 km. In the moment-tensor catalog of the University of Patras for the WGoC (Serpetsidaki et al., 2016, 2021), from 2006 to 2020 (before the crisis), only three events of Mw > 4.5 had centroid depth shallower than 5 km. In general, only a few earthquakes of Mw ∼ 5 worldwide, and not only in normal-faulting systems, have their slip localized at shallow depths ∼0–5 km (e.g., Champenois et al., 2017; Delouis et al., 2021; Ellsworth et al., 2019; Figueiredo et al., 2022; Liu & Zahradník, 2020; López-Comino et al., 2016; Wei et al., 2013). As some of them are shallow due to anthropogenic (triggered/induced) origin, the causative structures responsible for the very shallow slip of the natural Feb17 event above the rift detachment are worth studying. Compared with other earthquake sequences in WGoC, the low aftershock productivity of Feb17 is also uncommon. This sequence included ∼5 times fewer M ≥ 2 aftershocks than the sequences following the Mw 5.0 event of 7 November 2014, offshore Aigion (Kaviris et al., 2018) and ∼12 times fewer than those following the Mw 5.3 event of the 2010 Efpalio sequence.

Despite the abundant data provided by the CRL network, the association of the Feb17 event with one or more causative faults is challenging. Using all available data – including seismic waveforms, GPS, InSAR, and tidal gauges – we attempt to establish the rupture characteristics of the mainshock to assess a comprehensive picture of this atypical earthquake and its structural relationship with the rift fault system and the detachment layer.

The paper is structured as follows: A point-source modeling of the mainshock is carried out, yielding inconsistency between the relatively deep hypocenter, shallow centroid, and normal focal mechanism. To resolve the inconsistency, two-segment faulting is proposed involving both nodal planes, with weak nucleation at depth and a major moment release near the surface. Additional observational evidence and modeling are used to validate the model, including Empirical Green's Function modeling, backprojection, GNSS, Synthetic Aperture Radar Interferometry (InSAR), tide gauge data, Coulomb stress transfer, and microseismicity. Then, we correlate the proposed shallow causative fault with known structures of the Gulf. Finally, we discuss broader aspects of the Corinth rift faulting.

2. Seismic Single-Fault Model

2.1. Basic Data and Methods

Seismic data employed in this section consist of arrival times and full waveforms from local and near-regional networks comprising broadband, strong-motion, and short-period sensors. For the location of the mainshock and Mw 4 events, we manually re-picked P and S waves at 26 stations within distances of 27 km. The events were located with the probabilistic Oct-Tree method implemented in the NonLinLoc code (Lomax et al., 2001). The mainshock waveforms were analyzed at 13 stations at distances of 7 to 59 km; strong-motion records were used at stations where the collocated broadband sensor data was clipped. We employed the local 1D velocity model of Rigo et al. (1996), hereafter denoted as R-model; see Figure S1 in the Supporting Information S1. The model is based on seismic travel times and has been used in most previous earthquake studies of the region. Centroid

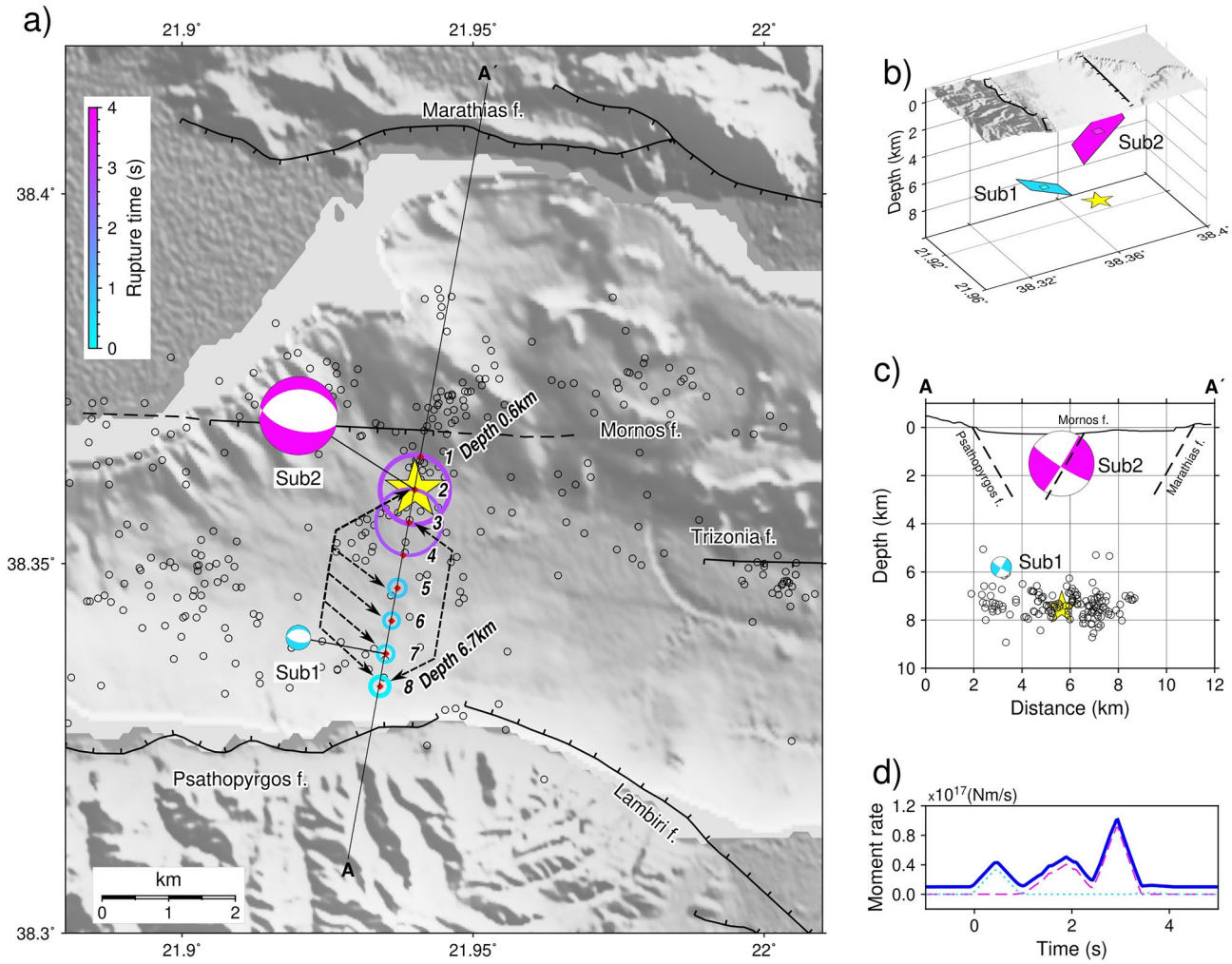

Figure 2. A two-segment source model of the mainshock. (a) Possible subevents Sub1 and Sub2 as found from a grid search of subevent pairs along an oblique trial line A-A'. The subevents (circles) at the trial source positions 1–8 are scaled with the moment and colored with the time of the peak moment rate. The individual subevent pairs are marked by the dashed lines with arrows that connect Sub1 and Sub2 of the alternative pairs; one of the subevent pairs is denoted by beachballs. Epicenter is denoted by star. (b) Conceptual view of an initial minor stage, Sub1 (cyan), on a low-angle north-dipping plane near hypocenter (star), and a later major stage, Sub2 (magenta), on a high-angle south-dipping plane near the surface. The two planes are conjugated. (c) The same model in a vertical cross-section and properly rotated beachballs; seismicity up to ±2 km off the section. (d) The moment-rate function (full line) with contributions of the two subevents (Sub1 cyan, Sub2 magenta). Also included in panels (a) and (c) is seismicity plotted with equal-sized small circles, i.e., the spatial group #3 of Figure S1 in the Supporting Information S1. This group has been defined in Figure 4 of Kaviris et al. (2021) and was mainly activated in the period of 17–28 February 2021. The subhorizontal seismo-active structure in panel (c) is the detachment layer. Major faults are included after Boiselet (2014), except the Mornos fault, which is plotted schematically following figure 9.1 of Beckers (2015) and will be in-depth analyzed later in Figure 9. Bathymetry from the European Marine Observation and Data Network (EMODnet), see Data Availability Statement.

moment tensors (CMTs) were calculated with the Isola software (Sokos & Zahradník, 2013; Zahradník & Sokos, 2018). Isola inverts full displacement waveforms for a point-source moment tensor (MT) by the weighted least-squares method. Various weighting schemes are used, e.g., weights dependent on epicentral distance, including total removal of a single station or their groups (randomly or systematically), and variations in the results contribute to the assessment of the uncertainty of the focal mechanism. The MT can be full, deviatoric, or DC-constrained. A grid search of the centroid is made in space and time, using various grids. As the centroid position (C) is calculated independently of the hypocenter (H), their relative position is useful in identifying which nodal plane is the fault plane (the H-C consistency concept; Zahradník et al., 2008). The consistency means that if we construct nodal planes passing through the hypocenter, the centroid should be situated in one of the two planes, or at least closer to one plane than to the other. The concept works well mainly for precisely located $M > 6$ events with a significant (~10 km) distance between H and C. In this paper, the H-C concept is used rather as

an indication, because the magnitude is smaller. The Isola software also includes tools for multiple-point source inversion, which will be discussed later.

2.2. Hypocenter

The Feb17 mainshock, located with the R-model, is at 21.94°E, 38.36°N, depth 7.9 km, with uncertainties of ±0.6 km and ±1.6 km in the horizontal and vertical direction, respectively; the origin time is 03:36:06 UTC. The uncertainties correspond to the 68% confidence ellipsoid fitted to the samples of the probability density (the samples form the 'clouds' plotted in Figure 1). For the ellipsoid, see Figure S4 of Kaviris et al. (2021). Hereafter, the likely hypocentral depth range of ~6–10 km, also valid for the largest foreshock and aftershock, is referred to as 'deep'.

2.3. Centroid

For a robust first approximation of the mainshock point-source model, we search for the centroid depth in a vertical grid below the epicenter, in the depth range of 1.5–8.5 km (Figure S1 in the Supporting Information S1), using the frequency range of 0.05–0.10 Hz at all stations. Here, the low-frequency limit is dictated by noise. The high-frequency limit of 0.10 Hz is chosen to reduce the effects of the imprecision of the velocity model; it means that in this range the departures of the model from real structure produce smaller waveform misfits than at higher frequencies. Indeed, the inaccuracy effect increases with the increasing ratio between the epicentral distance and shortest wavelength (e.g., Hallo & Gallovič, 2016; Zahradník & Sokos, 2018). For better understanding, consider an example: with the minimum shear velocity of 2.7 km at the topmost 4 kilometers in the R-model, the shortest shear wavelength is 27 km, and thus the most distant station (59 km) is at only 2.2 shortest wavelengths from the source.

The waveform fit of the deviatoric MT model is satisfactory (global variance reduction from 13 stations VR = 0.88). The MT features a high double-couple (DC) part, DC > 90%. Waveform data indicate centroid depths of ~1–4 km, a scalar moment ~1.0×10^{17} Nm (Mw = 5.3), and a focal mechanism with the strike/dip/rake angles in the range of (260°–290°)/(30°–40°)/(-100° to −80°), respectively. This uncertainty of the focal mechanism reflects varying trial depths and weighting schemes of the stations. The single solution reported by Kaviris et al. (2021), i.e., 266°/33°/-104°, conjugate with 103°/58°/-81°, is consistent with the indicated uncertainty range. This solution also fits most of the first-motion polarities. Analogous parameters can be obtained with a 100% DC-constrained MT inversion. At trial centroid depths near the hypocenter, the waveform fit deteriorates, and DC is below 50% (Figure S1 in the Supporting Information S1). A normal-faulting mechanism was also reported in the Global Centroid Moment Tensor, GCMT catalog (see Data Availability Statement).

A second approximation of the point-source model is searched in a series of 2D grids (5 × 5 points distributed horizontally with a 2-km step, centered below the epicenter), repeatedly applied at depths between 1.5 and 8.5 km with a 1-km step. Here, we use frequencies up to 0.1 Hz at 'distant' stations, between 26 and 59 km, and up to 0.2 Hz at 'near' stations at distances smaller than 26 km, to improve the spatial resolution. The best-achieved waveform fit is still satisfactory (VR = 0.78), the preferable depth being 1.5 or 2.5 km. The best-fitting horizontal position of the centroid is at the epicenter, or within ±1 km (Figure S1a in the Supporting Information S1). The location of the centroid above the hypocenter indicates an H-C inconsistency. If we construct nodal planes passing through the hypocenter, the centroid is off the two planes (Figure S1c in the Supporting Information S1). Therefore, a simple interpretation of the mainshock with both H and C lying in a single nodal plane (i.e., the fault plane) is hardly admissible. As such, the data cannot be explained with the rupture nucleating at H, propagating along a nodal plane, and evolving to a major slip at C on the same nodal plane.

3. Seismic Two-Fault Model

To alleviate the discrepancy between the hypocenter, centroid, and nodal planes, in the following we propose that the Feb17 mainshock consisted of two fault segments, as shown in Figure 2. We shall try to quantitatively support this *ad-hoc* (or on-purpose) hypothesis by modeling multi-parametric observations, starting with seismic data. We assume that both nodal planes are activated during the mainshock; the rupture process starts close to the 'deep' hypocenter on the north-dipping plane (the cyan area in Figure 2b) and ends with the major moment

release on the south-dipping plane at 'shallow' depths, near the epicenter (the magenta area in Figure 2b). The northward and southward dip of the planes will be justified later; it is not critical here as we consider the point sources.

The model is tested in the Isola software using multiple-point source (MPS) modeling of near-regional waveforms; specifically, we apply a joint inversion for subevent pairs and their moment-rate functions (see Appendix of Zahradník & Sokos, 2014). The source is parametrized with two points of given focal mechanisms. Hereafter, both have the same 100% DC focal mechanism based on our CMT. Moment-rate functions of the point sources are expressed as sets of shifted elementary functions (e.g., triangles) whose weights are calculated by the non-negative least squares method (Lawson & Hanson, 1974). Waveform fit at all stations is simultaneously optimized by systematically inspecting all possible pairs of points on a spatial grid. The method provides a suite of pairs with nearly equally good waveform fit. For methodical details and a recent application of the method, see Liu and Zahradník (2020). As the MPS inversion needs higher frequencies than CMT, it requires additional constraints. For this purpose, the total CMT moment value is kept fixed and trial source positions are searched on a line grid. The individual moments, positions, and moment-rate time functions of the two subevents are left free.

3.1. Subevent Pairs

We tested several geometrical configurations of trial source positions and frequency ranges to obtain robust results. Here we present an oblique trial source line that lies in the plane with strike/dip = 100°/60° and is orthogonal to the strike of the focal mechanism. The line is discretized with 8 grid points and 1-km steps, spanning depths from 0.6 km (trial point 1) to 6.7 km (trial point 8); see Figure 2a. To resolve the two sources, we inverted waveforms up to 0.1 and 0.3 Hz at the 'distant' and 'near' stations, respectively. Modeling frequencies higher than 0.3 Hz would need a more precise velocity model. In Figure 2a, we present a suite of subevent pairs that all provide a waveform fit within a 10% threshold relative to the optimal fit. In this suite, representing the model uncertainty, the following features can be identified: (a) An early weak rupture appears at depth (trial points 5–8); as the waveform fit does not significantly prefer any of these grid points, the early stage has a poor spatial resolution. This initial episode is hereafter referred to as subevent 1 or **Sub1**. (b) A relatively well-resolved late and large moment release occurs near the surface at trial points 2–3, called **Sub2**. (c) The moment ratio Sub1/Sub2 of the indicated pairs (Figure 2a) is 0.22–0.30. (d) When constraining the moment of Sub1 to zero, Sub2 remains at its shallow position. As an example, one of the possible pairs (subevents 1 and 2 at depths of 5.8 and 1.5 km, respectively) is shown in Figure 2 by beachballs; the moment ratio Sub1/Sub2 = 0.23. Resolved moments of Sub1 and Sub2 correspond to Mw 4.8 and 5.2, respectively. The waveform fit for this model is illustrated in Figure S2a in the Supporting Information S1. This is a tentative model supporting our two-segment hypothesis, where Sub2 is better constrained than Sub1. When removing Sub1, waveform fit is only slightly worse (Figure S2b in the Supporting Information S1). The situation is similar to that in Figure 4 of Frietsch et al. (2021) who note that visual comparison of waveforms for single-fault and two-fault models is not very efficient when one of the subevents is significantly greater than the other. It means that our waveform data do not necessarily require the Sub1 but they allow for its presence at depth, which was strongly suggested by the hypocenter location. However, when modeling our earthquake with just a single patch constrained to the depth of 7.5 km, waveform fit is significantly worse due to the absence of the dominant shallow moment release (Figure S2c in the Supporting Information S1).

The moment-rate function is demonstrated in Figure 2d. The time function is calculated as a linear combination of delta functions with non-negative weights. With the maximum frequency of 0.3 Hz, each delta function is approximately equivalent to a triangle of an effective duration T, where $0 < T < 3$ s. The largest weights determine the individual source episodes. For instance, Figure 2d shows an early, relatively weak rupture of the deep trial point 7, close to $t = 0.5$ s (relative to origin time at $t = 0$), followed by two larger moment-release episodes in shallow point 2 at $t \sim 2$ and 3 s. For illustration, we plotted the moment rate as superposed from triangles with $T = 1$ s, thus estimating the duration as 3.5 s.

3.2. Fault Planes

In our waveform modeling, both proposed point-source subevents have the same focal mechanism, that of the CMT. There was no reason to propose mixed-type faulting. Mixed faulting styles may include, for example, superposition of strike-slip and normal faulting (Hallo et al., 2017; Tinti et al., 2021), or strike-slip and reverse

faulting (e.g., Hallo et al., 2019; Liu & Zahradník, 2020; Sokos et al., 2020). They are often indicated by large compensated-linear-vector-dipole (CLVD) components, which is not our case, as we obtained the deviatoric CMT with DC ∼100%. To keep the same normal-faulting focal mechanism of the subevents, but to respect their different depths, we propose that Sub1 and Sub2 ruptured the conjugate nodal planes, i.e., the low-dip and high-dip planes, respectively, as shown by the cyan and magenta small surfaces plotted in Figure 2b. The reasons for this assumption are: (a) Geometrically, the best-fitting planar approximation of many foci situated on the Corinth Rift detachment was found to agree with the low-angle nodal planes (Rietbrock et al., 1996). (b) A low-angle fault plane has been preferred for the Mw 6.3 Aigion 1995 earthquake, with hypocentral and centroid depths of 10 and 7.2 km, respectively (Bernard et al., 1997). (c) Comparing our CMT nodal planes with the nearby high-angle north-dipping Psathopyrgos fault and the low-angle detachment (Figure 2c), the latter is more likely at the assumed deep position of Sub1. (d) The low-angle nodal plane of Sub1 passes near the hypocenter, thus meeting the H-C consistency criterion in the initial rupture stage. 5) The high-angle south-dipping plane of Sub2 is acceptable at shallow offshore depths in the studied region (De Barros et al., 2020).

4. Finite-Extent Model of the Shallow Slip

4.1. Apparent Source Time Functions (ASTFs)

Finite-source signatures of the major near-surface rupture (Sub2), that appear in waveforms at relatively high frequencies (∼1 Hz) cannot be resolved by synthetic modeling. At these frequencies, we would need a more precise velocity model than available. Instead, for a finite-extent source model, we apply the empirical Green's functions method, EGF (Figure 3). As opposed to common frequency-domain deconvolution methods, we work fully in the time domain. At each station, the mainshock record is expressed as a weighted linear combination of records of a small event, the so-called EGF event. The apparent source time function (ASTF), or moment-rate time function, having the same area (i.e., total seismic moment) at all stations, is parametrized with equally shifted triangles. The weights are calculated by a non-negative least-squares inversion of waveforms, as shown in Figure S3 of the Supporting Information S1. Our inversion is performed on band-pass filtered waveforms in the range of 0.1–1.0 Hz and the duration of the triangles is set to 1 s. The used low-frequency limit is dictated by noise in the EGF event, and the high-frequency limit compromises the space resolution and stability of the subsequent inversion of ASTF for slip. Finding a suitable EGF event is a challenge because seismicity around Feb17 was lower than during the previous stages of the 2020–2021 activity. Fortunately, there is a nearby, normal-faulting foreshock, Mw 4.2 (20210217, 02:33, 21.9479°E, 38.3632°N, hypocenter depth 8.9 km, strike/dip/rake = 255°/39°/-105°, Figure 1). Employing this EGF event, the inferred ASTFs, shown in Figure 3a, reveal a clear azimuthal variation. Minimum durations and maximum amplitudes are encountered in the azimuths N80°E - N100°E, suggesting an eastward source directivity. It means that Feb17 is directive in the horizontal direction, as analogously observed in other normal-faulting environments, e.g., in the Apennines (Calderoni et al., 2017; Pacor et al., 2016; Pino & Mazza, 2000). The mean ASTF duration of 3.3 s is compatible with the previous estimate from the MPS modeling.

4.2. Slip Distribution

Further, these ASTFs are inverted into a slip-distribution model using the method of Mori and Hartzell (1990) and the STF inversion code of Dreger (1994). A predefined planar fault is divided into uniform subfaults. The slip-rate function of each subfault is a triangle of predefined duration (rise time, τ). Slip at each subfault is calculated under the assumption that the rupture propagates radially from the specified nucleation (initiation) point, at a constant speed Vr. Values of Vr and rise time τ are searched to optimize the match between observed and synthetic ASTFs, which is quantified by variance reduction. We assume a fault much larger than the assumed slip patch, i.e. 19 × 15 km along strike and dip, respectively, gridded with 1 × 1 km subfaults.

As a preliminary step, in Figure S4 of the Supporting Information S1 we first test both geometries inferred by our CMT solution, i.e. the north- and south-dipping faults. The two faults are passing through the hypocenter (depth 7.5 km), and rupture is initiated at that point. The largest variance reduction is achieved for Vr = 2.7 km/s and τ = 1.0 s, almost identical for both tested planes (VR ∼ 0.94). The ASTFs inversion provides slip weights for the considered subfaults, which are converted to slip values using a prescribed seismic moment (in our case the CMT moment of 1.0×10^{17} Nm). In the tested models, ∼90% of slip appears concentrated in an area of ∼30 km^2 with

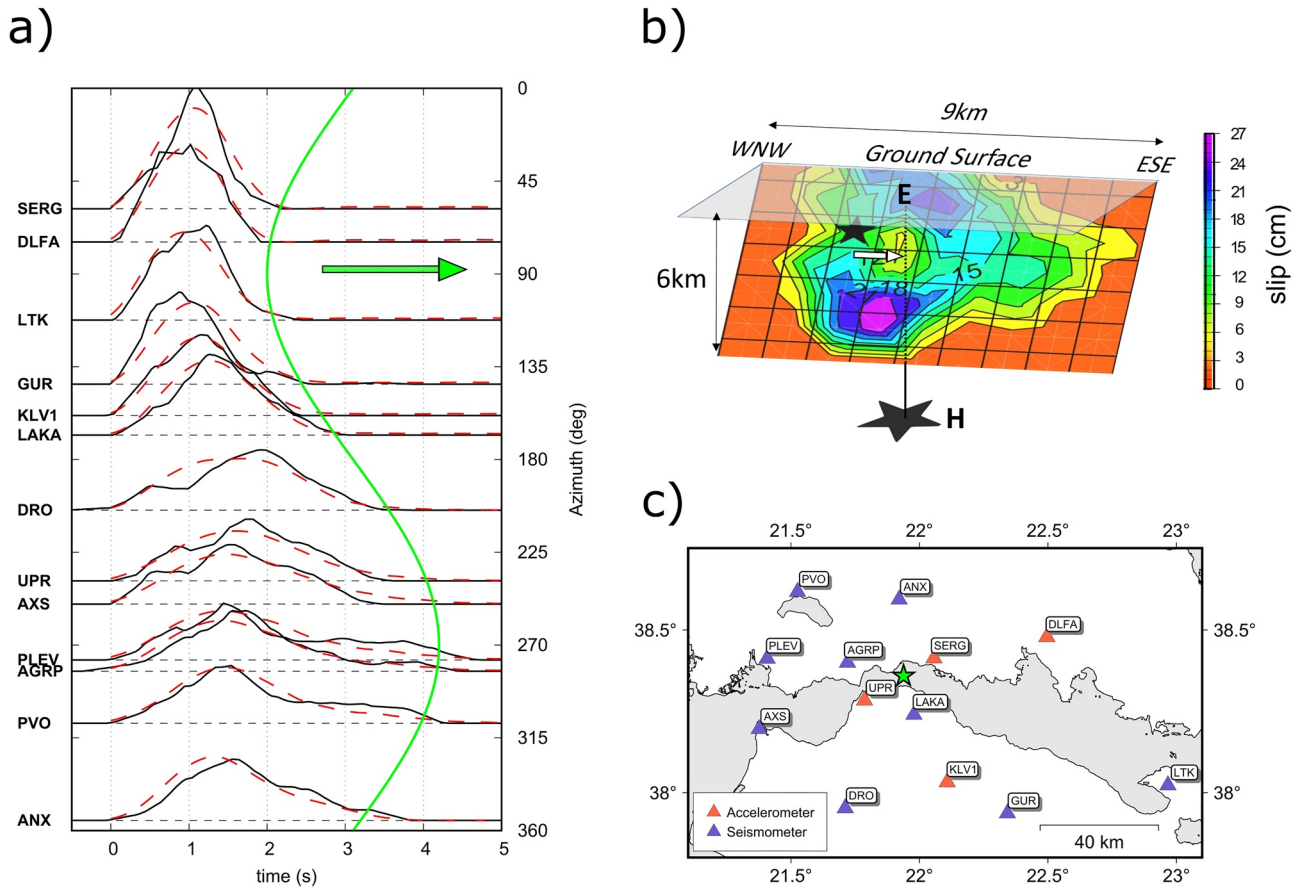

Figure 3. Finite-extent modeling of the shallow rupture. (a) Apparent source time functions, ASTFs, for frequencies up to 1 Hz derived by the empirical Green's function method, EGF (full black lines). Azimuthal variation of the durations around a ~3-second mean is well fitted by an eastward-directivity model (the green cosine curve and the arrow pointing to the directive azimuth of ~90°). (b) Slip patch derived by inverting the ASTFs on a south-dipping plane (the Sub2 plane of Figure 2b). The mean slip is ~15 cm. The model has been constrained by the CMT solution to have the center of the patch (centroid) situated at a shallow depth below the epicenter (E). The small star on the fault depicts the inferred (possibly formal) shallow rupture initiation point. The short white arrow between the small star and the patch center in panel b is a schematic of the source directivity. The large star marks the hypocenter (H). Synthetic ASTF's for this model are shown in panel a (dashed red lines). (c) The employed seismic stations.

a mean slip close to 15 cm. In both slip distributions, the slip appears mostly to the east of the hypocenter and is confined at depths larger than ~6 km. This solution with a deep slip thus contradicts the well-constrained shallow centroid depth of the CMT, so the hypothesis of a rupture initiation at the hypocenter should be rejected. It means that the dominant, radiative part of the rupture could not simply expand near the hypocenter.

A more realistic model (than that in Figure S4 of the Supporting Information S1) can be obtained when considering that this slip inversion method only reveals a slip distribution relative to the adopted nucleation point, as the mainshock and EGF event records are aligned to their first-arrival times. Thus, to the first order, shifting the nucleation point results in shifting the slip pattern as a whole, keeping their relative position accordingly. Therefore, as a second step, we apply the prior CMT constraint of the shallow centroid above the hypocenter. We cannot improve the waveform fit compared to the preliminary step but can obtain the same fit (VR = 0.94) with slip distributed at shallow depths ~0–5 km. To this goal, we assume a nucleation point at a mid-depth, 2.5 km, see the small star in Figure 3b. Now we satisfactorily fit the observed ASTFs (VR = 0.94 in Figure 3a), while the resulting slip is distributed at depths 0–5.5 km, consistent with the shallow centroid depth. The eastward shift of the patch relative to the nucleation point (Figure 3b) explains the observed azimuthal variation of the ASTFs (directivity). The split of the slip patch in two maxima is probably an artifact due to the effect of the weak initial Sub1, which cannot be removed from the inverted ASTFs.

It is noted that the shallow nucleation point in Figure 3b is not the earthquake hypocenter, but a point that we inferred as a suitable representation of the initiation of the shallow rupture, Sub 2. We can consider that point

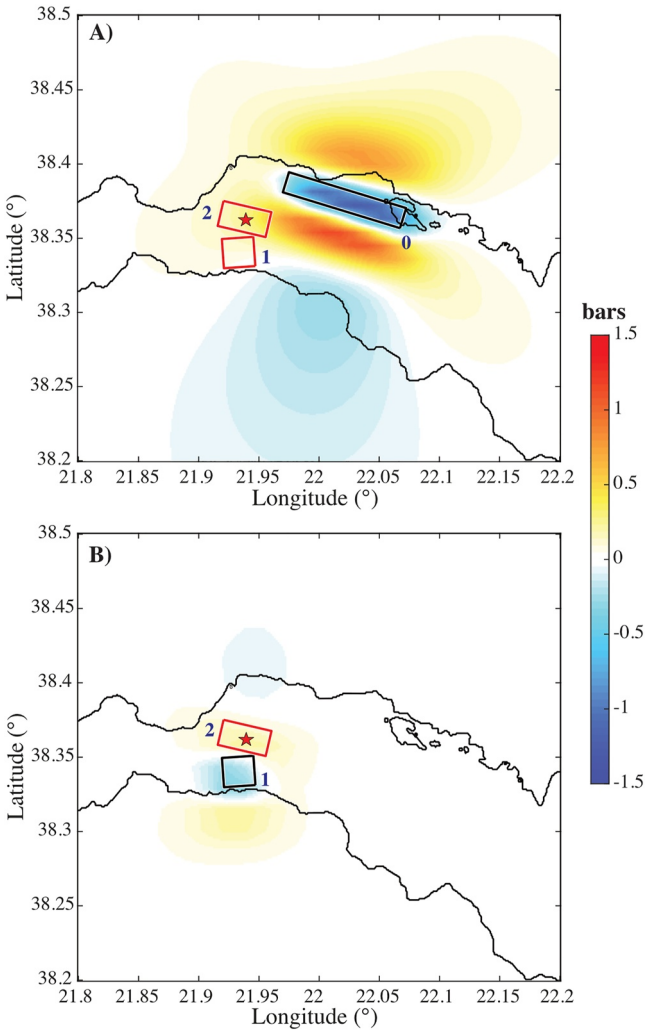

Figure 4. The Coulomb stress transfer. (a) The Coulomb stress (bars) due to the Mw 5.0 earthquake of January 2021 (fault 0), resolved at optimally-oriented normal faults at depth of 2 km. Rectangles 1 and 2 depict subevents Sub1 and Sub2 of the February 17 mainshock. (b) The Coulomb stress (bars) due to Sub1, resolved on the assumed fault plane of Sub2. Star is the epicenter of the Feb17 event.

as a 'second hypocenter' (in analogy with Gallovič et al., 2020), but in the Feb17 event, it cannot be reliably detected in seismograms. Thus, compared to the relatively well-constrained horizontal position of the centroid from the CMT inversion (~ center of the slip patch), the existence and position of the proposed shallow nucleation point (the small star in Figure 3b) at ~1 km WNW of the centroid cannot be independently validated.

4.3. Coulomb Stress

To justify the shallow slip of the Feb17 event, we analyze in Figure 4 the static Coulomb stress transfer ΔCFS. We use the code Coulomb3.4 (Lin & Stein, 2004; Toda et al., 2005, 2011) and calculate $\Delta CFS = \Delta\tau + \mu\,\Delta\sigma$, where $\Delta\tau$ is the shear stress change (positive in slip direction), $\Delta\sigma$ is the normal stress change (positive for unclamping), and μ is the friction coefficient. We assume an elastic half-space characterized by the standard values of Poisson's coefficient, Young's modulus, and the friction coefficient of 0.25, 8×10^5 bars, and 0.4, respectively, together with the regional stress field for the Corinth Gulf area (Kassaras et al., 2016). Two causative faults are considered: (A) The stress-generating fault is the fault of the Mw 5.0 earthquake of 12 12 January 2021 – the largest event of the crisis on the northern coast, i.e., the second biggest magnitude event during the crisis. The fault model of this event is represented in Figure 4a, as proposed in Figure S2 of Kaviris et al. (2021). (B) The stress generating fault is the deep nucleation segment Sub1 of our Sub1-Sub2 model.

We proceed in three steps. First, in Figure 4a, the Coulomb stress due to fault A is resolved at optimally oriented normal faults at the depth of 2 km. Irrespective of the exact position and geometry of the target fault, elevated stresses are indicated near the epicenter. Second, we use the same generating fault (A) and consider receiving fault Sub2, with its position, size, and focal mechanism. This gives the Coulomb stress of ~0.3 bars on Sub2. Third, in Figure 4b, the Coulomb stress due to fault B is resolved on the Sub2 fault plane, again considering its position, size, and focal mechanism. This adds another 0.3 bars on Sub 2. Thus, the total stress increase on the shallow Sub2 plane, due to the combined effect of the major north-coast January 12 event and the deep nucleation Sub1, i.e. A plus B, is estimated as 0.6 bars.

5. Further Validations of the Two-Fault Model

Here we apply additional data and techniques to further examine the herein proposed two-segment hypothesis. First, we investigate the mainshock rupture kinematics with the near-regional seismic backprojection method modified from Evangelidis (2015).

5.1. Backprojection of Seismic Waveforms

The Source-Scanning Algorithm (SSA) (Kao & Shan, 2004, 2007) has been implemented for the identification of the spatio-temporal evolution of the Feb17 event. For this analysis, eight strong-motion and three broadband stations within ~50 km epicentral distance have been selected, as shown in Figure 5a. We process this dataset by applying a 2–8 Hz bandpass filter and converting waveforms to envelopes. A 4-D spatial-temporal grid with a 1-km spatial and 0.1-s temporal step is employed. For each point and time, the brightness function is calculated by stacking the waveforms based on the expected S-wave travel times. To reduce the effects of velocity-model inaccuracies, instead of waveforms we use their envelope amplitudes averaged in a time window of 0.3 s around the expected arrival. As such, large brightness function values (bright-spots) are likely to emerge at space points and times close to real radiators of the high-frequency (HF) waves, tracking the rupture propagation process. As

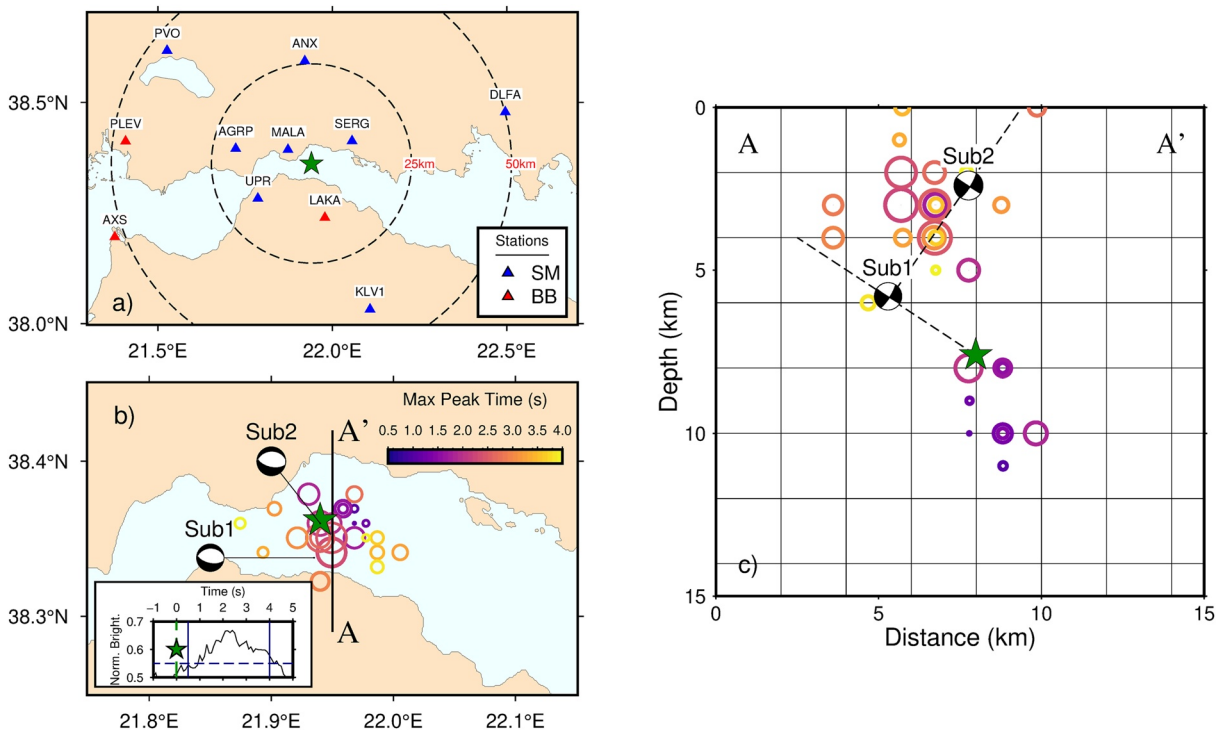

Figure 5. Seismic backprojection - maximum brightness locations in space and time. (a) Strong-motion (SM) accelerometer and broadband seismometer (BB) stations used in this method; distance circles at 25 and 50 km from the epicenter (star) are presented by dashed lines. (b) Bright spot locations plotted as circles colored with time and sized proportionally to maximum brightness values; suggested subevents Sub1 and Sub2 are shown for comparison. The normalized maximum brightness variation with time is presented in the inset. Shown by a horizontal dashed line is the amplitude threshold below which the brightness is neglected for stability reasons. (c) The N-S vertical cross-section along profile AA' is shown in panel (b) Star is the hypocenter. The dashed lines indicate the two proposed fault planes.

illustrated in Figure 5b, for this earthquake, the brightness function starts to rise shortly after the origin time, attends a maximum at ~2.3 s later, and has an overall duration of ~4 s. Spatially, the HF energy is released initially in the area around the hypocenter and then migrates ~1.8 s later to shallower depths and slightly southward.

To assess the resolution of the applied method we also performed synthetic tests; the two most important of them are shown in Figure S5 of the Supporting Information S1. First, we forward simulated noise-free seismograms for two subsequent point sources in a layered velocity model, each one of a 2-second duration (located in the assumed positions of subevents Sub1 and Sub2). Using the same velocity model, the backprojection method successfully retrieved the temporal complexity. The spatial position of the subevents was horizontally smeared in their neighborhood yet successfully retrieved vertically. Secondly, a simpler test (equivalent to the array response function) was performed with a single source in the hypocenter. In this test, we observed an almost ideal image of the source, without major artifacts, with just a very small (negligible) E-W drift. This test confirmed the suitability of the station coverage and indicated that the scatter of bright spots in the first test is due to the complexity of the source process.

Comparing real-data analysis in Figure 5 with the synthetic tests in Figure S5 of the Supporting Information S1, we find a closer similarity with a two-source test, yet the real-data time function indicates a rather continuous temporal evolution (instead of two individual separate events). Therefore, the backprojection method is in general agreement with our two-fault hypothesis. Indeed, the vertical cross-section in Figure 5c confirms the start of the source process (Sub1) at the hypocenter depth of ~8–10 km followed later by the shallow dominant rupture episode (Sub2) at a depth of ~2–4 km.

5.2. GNSS and InSAR Data

To strengthen the seismic indication of shallow slip, we add also geodetic data. We compare the geodetic prediction of our source model with updated static displacements values at GNSS stations, which were newly

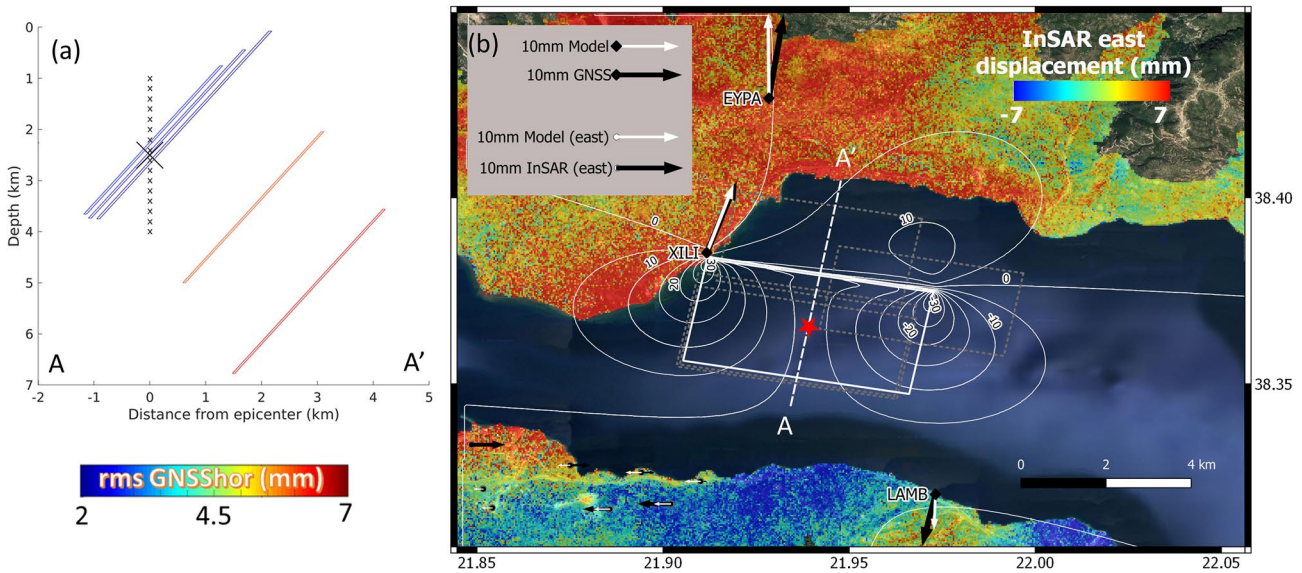

Figure 6. GNSS-horizontal and InSAR-east data. (a) Cross-section AA' (also in panel b) of the modeled south-dipping fault planes and the root-mean-square (rms) misfit of GNSS. The best-fitting planes (blue) are centered around a 2–3 km depth. Large and small cross (×) symbols, forming a vertical line in panel a, depict seismic centroid and its uncertainty, respectively. (b) The InSAR-east displacement component is color-coded, while the synthetic displacement model is shown with iso-displacement contour lines (labeled in millimeters). Projections of the rectangular faults (from panel a) are shown by white dashed and solid lines. The latter highlights the best-fitting fault centered below the epicenter (star). Diamonds depict the three GNSS sites of the dominant displacement, LAMB, XILI, EYPA. Small circles on the south coast depict the eight highest-coherence points of InSAR data. For the arrows, see the inset.

determined by exploiting a ∼1-year time series after the event, longer than in Figure 3 of Kaviris et al. (2021). Additionally, for InSAR processing, we use the available SENTINEL-1 acquisitions with the tropospheric noise minimized and the common mode signal amplified.

Static horizontal GNSS displacements ≤14 mm (with uncertainties ± 2 mm) produced by the Feb17 event were preliminarily interpreted as the slip on a rectangular north-dipping fault, centered at a depth of ∼2.5 km (Kaviris et al., 2021). Vertical GNSS data have lower accuracy. Here we re-examine the horizontal GNSS data and confirm that they indeed imply a slip at shallow depth. The geodetic data allow for a variety of fault positions and geometries, including the south-dipping fault – i.e. our hypothetical shallow subevent (Sub2), as illustrated in Figure 6a. As the ground displacement is dominated by the shallow source, the geodetic data cannot constrain the minor, deeper nucleation subevent (Sub1).

We complemented the GNSS records with InSAR data. Twelve Sentinel-1 acquisitions were used before and twelve after the Feb 17 earthquake, belonging to ascending and descending tracks. To avoid mixing with the deformation produced by the January 12 event, the first used acquisition is from one day after that event. For the ascending track, 175, the first one was acquired on January 13, at ∼04:40 UTC, and for the descending one, 80, on the same date at ∼16:30 UTC. All the succeeding acquisitions were separated by six days. Thus for each track, six acquisitions were dated before and six after the earthquake. From these data, 72 interferograms were produced with the Diapason service of the European Space Agency's Geohazard Exploitation Platform (GEP), see Data Availability Statement. The processing included: selecting the interferograms with adequate coherence, correcting for the stratified and turbulent tropospheric noise using zenith tropospheric delays from the Generic Atmospheric Correction Online Service for InSAR (GACOS), (Yu et al., 2017; 2018a; 2018b), removing the relative offset using the most coherent and low altitude pixels, masking the sea manually, unwrapping using Statistical-Cost, Network-Flow Algorithm for Phase Unwrapping (SNAPHU) software (Chen & Zebker, 2002), averaging, calibrating with the GNSS and decomposing into two line-of-sight displacements (Dalla et al., 2012), and finally extracting the east and vertical displacement components. The full chain processing was performed separately for the north and south coast, revealing the InSAR east-component uncertainty of ±4 mm and ±3 mm, respectively. The InSAR vertical components are not considered here because they might be affected by post-seismic secondary ground motion, for instance, due to underground sediments compaction of deltaic areas (Briole et al., 2021; Elias & Briole, 2018). The areal distribution of the InSAR east displacement is shown in Figure 6b.

For quantitative modeling, we selected the InSAR east data just at eight highest-coherence points from the south coast (each one extracted by averaging 16 nearest scatterers at a maximum distance of 80 m). These data were merged with the horizontal GNSS data, and their modeling was performed with the Inverse6 code (Briole, 2017), using the method described by Briole et al. (1986). The inversion is mostly controlled by the three nearest GNSS stations because the selected InSAR data have unequal distribution and larger uncertainty (Figure 6b). In a series of performed tests, designed to check the feasibility of south-dipping faults (strike/dip/rake = 100°/50°/-90°), we inverted for the fault position, dimension, and uniform slip. The lowest root-mean-square (rms) misfit of the GNSS data (rms = 2.1 mm) and the InSAR east data (rms = 3.4 mm) were found for the shallowest faults centered at a depth of 2–3 km, near the seismic centroid (Figure 6a). A similar fit to geodetic data was also obtained with shallow low-angle north-dipping faults; such solutions are not discussed here because, as shown later, they are not supported by geological data.

In Figure 6b the InSAR east component can be qualitatively compared with modeling. We observe a remaining tropospheric noise but it is within the uncertainty level of the observed displacements. Considering the low signal-to-noise ratio, the discrepancy between the model and the InSAR east component is within an expected range. The same inversions solely with GNSS data led to the same results, i.e. the faults centered at a depth of 2–3 km, confirming the robustness of the procedure as well as the small contribution of the InSAR data. The center of the best-fitting fault is projected to surface at 21.939°E, 38.365°N, i.e. near the Feb 17 epicenter. The moment is 1.2×10^{17} Nm, typical along-strike and along-dip fault lengths are 5.0–5.5 km, and 4.5–5.0 km, respectively, and uniform slip ∼15 cm, compatible with the seismic model. This implies that aseismic, short-term postseismic moment release on this fault, if any, is smaller than the coseismic moment release. Finally, note that the fault centered at the depth of 2–3 km is in agreement with seismic backprojection where major brightness spots appear between depths of 2 and 4 km.

5.3. Tide Gauge Data

Obviously, an Mw 5.3 earthquake could not generate a strong tsunami enabling a detailed characterization of the faulting process. Nevertheless, a small tsunami was observed, which is used for partial validation of the proposed shallow slip model.

Two tide gauges located in the Corinth Gulf recorded sea-surface variations caused by the Feb17 mainshock, with a crest-to-crest amplitude of ∼5 cm at the Monastiraki (MOKI) station of CRL, 5 km north of the epicenter, and ∼4 cm at the Aigion (AIGI) station of the Intergovernmental Oceanographic Commission (IOC), 17 km to the south-east (Figure 7). We compare this signal with the one produced by trial source faults of the 5.6 km length, 3.5 km width, striking N103°E and dipping 58° to the south, with a uniform 15 cm slip of rake −81° and varying the fault-center depths from 2.5 to 7.0 km. The tsunami modeling is based on the calculation of static displacement on the surface of a homogeneous elastic half-space caused by an assumed instantaneous rectangular dislocation (Okada, 1985), transformed through the water column as described in Glimsdal et al. (2013). We propagate the resulting tsunami wave according to the nonlinear shallow water equations in a Cartesian coordinate system (e.g., Heinrich et al., 2021), using the European Marine Observation and Data Network (EMODNET) bathymetry through the WGoC ("mother grid") and the Navionics nautical charts close to the Monastiraki Bay ("refined grid"), see Data Availability Statement and Figure S6 in the Supporting Information S1.

MOKI station (Figure 7, panels b and d) is situated in the near-field of the source and records the sea level with a 1 Hz sampling frequency, which makes it less prone to aliasing. The waveform is thus better recorded, yet accurate simulation requires refined bathymetry. Indeed, the MOKI station is situated in a small bay that is prone to numerical oscillations, while the real oscillations are attenuated due to their small signal-to-noise ratio. As a result, simulated and observed time series rapidly diverge (after a few minutes). However, as tsunami wavelength mainly depends on the coastal shape for comparable fault sources, we mostly look at the first wave polarity, to confirm the focal mechanism compatibility, and the crest-to-crest amplitude, depending on the source depth, the amount of slip, and the attenuation of the waves. On the other hand, the AIGI station (Figure 7c) being more distant and only sampled at 16.6 mHz, is more robust but less discriminating.

The observation of a rapid sea-level oscillation at MOKI station 2 minutes before the arrival of the first major wave, identified as the immediate response to the seismic waves, enables anchoring the time t = 0 of the tsunami simulation, thus avoiding any clock error larger than a few seconds. As a consequence, the simulation reproduces

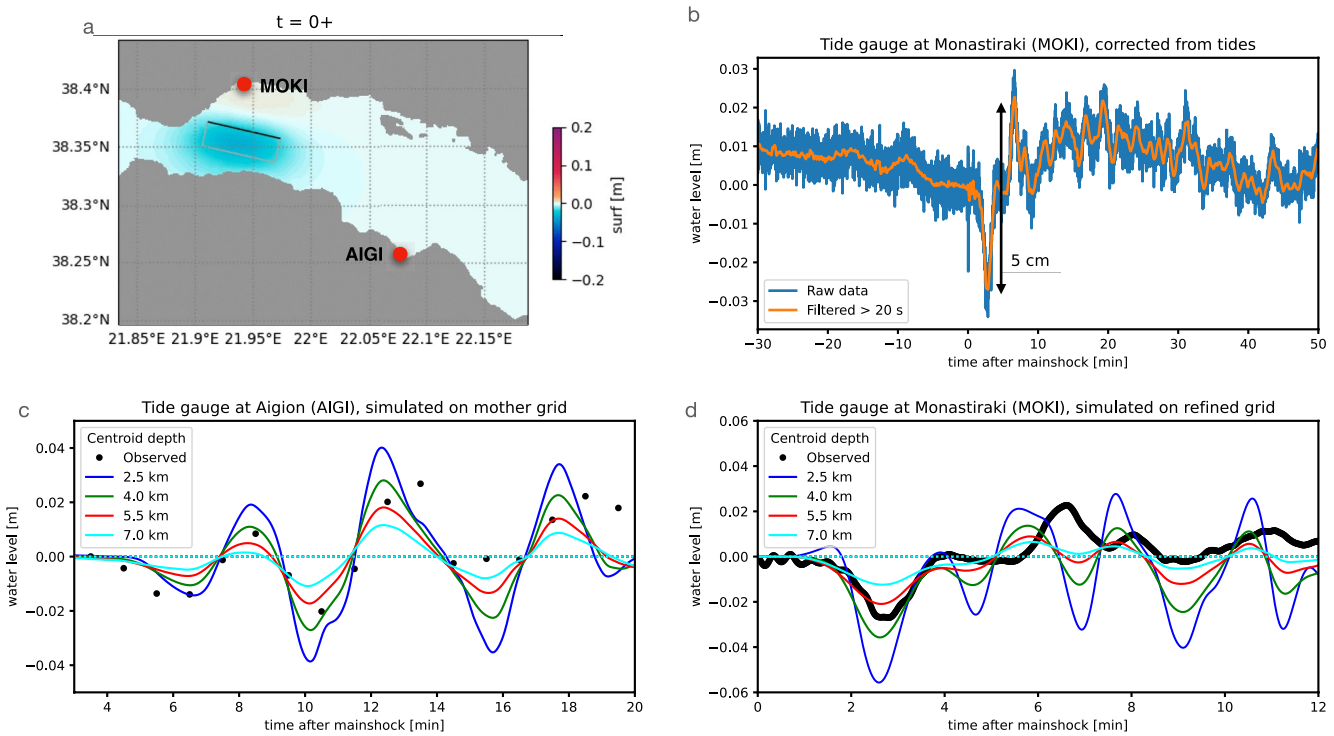

Figure 7. Tide gauge data. (a) Two tide gauges, the fault model, and simulated water level at time t = 0+, i.e., immediately after the dislocation. (b) Observed sea level variations at MOKI station, corrected from first-order tide cycles (raw and filtered data, see the legend). (c) Examples of simulated water variations at AIGI station on the mother grid, compared with ∼1-min sampled real data. (d) Examples of simulated water variations at MOKI station on the refined grid, compared with 1-sec sampled real data. The finely sampled observed points appear as a black solid line. See Figure S6 for details and the link in Data Availability Statement for animation.

the tsunami travel time for the two stations, validating both the propagation model and the epicenter location. Moreover, both stations show a compatible first waveform, starting with a downward motion, which tends to confirm a predominantly normal focal mechanism. The modeled amplitudes in both stations rule out a centroid deeper than ∼ 6–7 km; indeed, a centroid at such depths would not be detected by the existing tide gauges. On the other hand, ruptures with centroid shallower than 3 km are also less likely as they would imply amplitudes significantly greater than those observed. Therefore, the best-fitting depths of fault centers to simulate the tsunami waves in the assumed source model are in the range of 3–5 km. Thus the tidal variations, GNSS data, and back-projections agree with each other at the ∼ 3-km depth of the likely shallow source center.

5.4. Microearthquakes – Foreshocks and Aftershocks

Finally, we relocate abundant microearthquakes in a close space-time vicinity of the mainshock. We shall show that practically all the activity concentrated near the deepest part of the seismic process of the Feb17 event (Sub1), not only including foreshocks but also aftershocks. While Kaviris et al. (2021) presented a seismic catalog based on manual picks and absolute locations, here we adopt a different method – we produce a catalog based on automatic picks and relative relocations. Thus we can analyze a large number of events that better illuminate the geometry of the seismically activated structures.

Automatic picking of P and S arrival times was performed for sixteen stations up to epicentral distances of ∼25 km using the deep neural network algorithm Phasenet (Zhu & Beroza, 2019). The event association was performed with the associator REAL, based on a grid search (Zhang et al., 2019). The association was followed by the initial absolute location using VELEST code (Kissling et al., 1995), starting from the R-model (Rigo et al., 1996). A local (Richter's) magnitude was also estimated. Next, cross-correlation was computed between all pairs of events in a time window of 5.12 s (starting 1 s before the P-wave) at all stations and all available channels. If the correlation coefficient at eight or more stations was higher than 0.7, which is our threshold, the two events were merged into the same group, and their waveforms were stacked. The groups of more than three events were used for template matching detection (Lengliné et al., 2016). The final stage consisted of calculating

differential arrival times for all these pairs of events on the P- and S-wave. Windows of 1 and 3 seconds were used for the P- and S-waves, respectively, and records were filtered between 2 and 30 Hz. These differential arrival times were used to relocate the events with the Growclust software (Trugman & Shearer, 2017). Relocation uncertainties for the earthquakes between 16 and 19 February have been estimated using the bootstrap procedure of the latter software. The 50 runs of the code with a resampled data vector led to a mean uncertainty of 217 m horizontally and 277 m vertically. In total, the catalog contains 98095 events for the period from 22/12/2020 to 28/02/2021 (see Data Availability Statement). In this set, 15871 events, including mainshock and the largest foreshock and aftershock could not be relocated, because their waveforms did not correlate with other events within the adopted threshold. These events were assigned the initial location or the location of the template event that detected them.

Here, we use the new catalog to analyze the relocated microseismicity in the vicinity of the Feb17 event. In Figure 8a we demonstrate that the seismicity within 24 h before the mainshock covered a broad region east of the epicenter (representing migration from the north coast), but the foci distribution pattern was sharply limited or stopped at its western end, just near the hypocentral zone of Feb17. In 24 hours after the mainshock, the seismicity was boosted and concentrated in an ~8 × 8 km region. This boost was approximately omnidirectional, including a westward spread of the activity, beyond the limit of the previous day. Thus we focus on a specific region (see the large red rectangle in Figure 8a) which is further illustrated in Figures 8b and 8c. We find the following: 1) Within 24 h after the mainshock, a region free of aftershocks (a gap) appeared near ~38.36°N, 21.92°E. This region can mark the proposed initial deep rupture stage (Sub1) of our hypothetical two-segment mainshock model. 2) A properly chosen closer 3D view (Figure 8c, and Figure S7 in the Supporting Information S1) shows that the gap is surrounded by four clusters (1–4) active during the day after the mainshock, while only one of the clusters (no. 1) was activated already during the previous day. The clusters can indicate off-plane aftershocks of the Sub1 stage, caused by stress load from Sub1. The gap is robust relative to location errors (Figure S8 in the Supporting Information S1). 3) A planar 3 × 3 km fault segment, with a strike ~260° and dip ~30° as proposed for Sub1 in our two-fault hypothesis, is compatible with the gap defined by the four clusters near its corners. This small aftershock gap could be geometrically fitted by a subhorizontal plane (dip ~ 10°), indicating a possible relation of the initial mainshock stage to the detachment surface. 4) Vertically, the thickness of the observed micro-seismically activated zone is about 3–4 km. This zone can be considered as the bottom limit of the proposed shallow major slip patch (Sub2) if the latter extends down to ~5–6 km (Figure 3b).

Very few aftershocks of the first 24 hours are detected above the massively activated microseismic zone; there are just six events at depth <5 km in the cross-section of Figure 8b (i.e., within ±4 km laterally from the indicated profile A-A'). For another vertical cross-section, see Figure 9. As already mentioned, the mainshock, as well as the major foreshock and aftershock could not be relocated by the methods of this section; it is because their waveforms are poorly correlated with smaller events. Thus we can neither confirm nor reject their shallow depths. Their absolute hypocenter locations are rather similar to the mainshock (Figure 1).

The above-presented interpretation speculated about the possible small aftershock gap between four clusters; the gap was fitted by a small fault segment in agreement with the focal mechanism of the initial deep rupture episode (Sub1) on the north-dipping nodal plane. Nevertheless, the relocated events allow for various (non-unique) formal planar approximations. In Figure S7 of the Supporting Information S1 we also emphasize the overall main trend of the seismicity in a longer time interval (up to 10 days after the mainshock), and within a larger region (between 21.88°E and 21.96°E). Here we can fit very well the foci distribution by a south-dipping planar segment ~11 × 8 km, extending between depth ~6–10 km, and featuring strike/dip = 100°/50°. We recall that strike/dip = 100°/50° is a typical fault geometry for the north coast of the Gulf (De Barros et al., 2020). Nevertheless, despite the strike and dip mimics our Sub2, the south-dipping structure revealed in Figure S7 of the Supporting Information S1 should not be confused with Sub2 of our two-segment hypothesis, as Sub2 is shallower. Instead, we propose that deep microseismicity in Figure S7 of the Supporting Information S1 reveals a root of a south-dipping high-angle normal fault, analyzed in the following discussion and Figure 9.

It is difficult to correlate the relocated foci with fault structures. Strictly speaking, although several planar approximations are formally possible, none of them may be physically valid. Detachment is a complex, highly fractured, medium where a simple concept of 'fault plane' should be considered with caution, particularly when explaining just the small initial phase of the mainshock. Clusters of foci are not observed to align along with a well-defined structure but show multiple shorts segments with various orientations. They may also only highlight small areas of stress concentrations or areas with mechanical weaknesses, such as fault intersections.

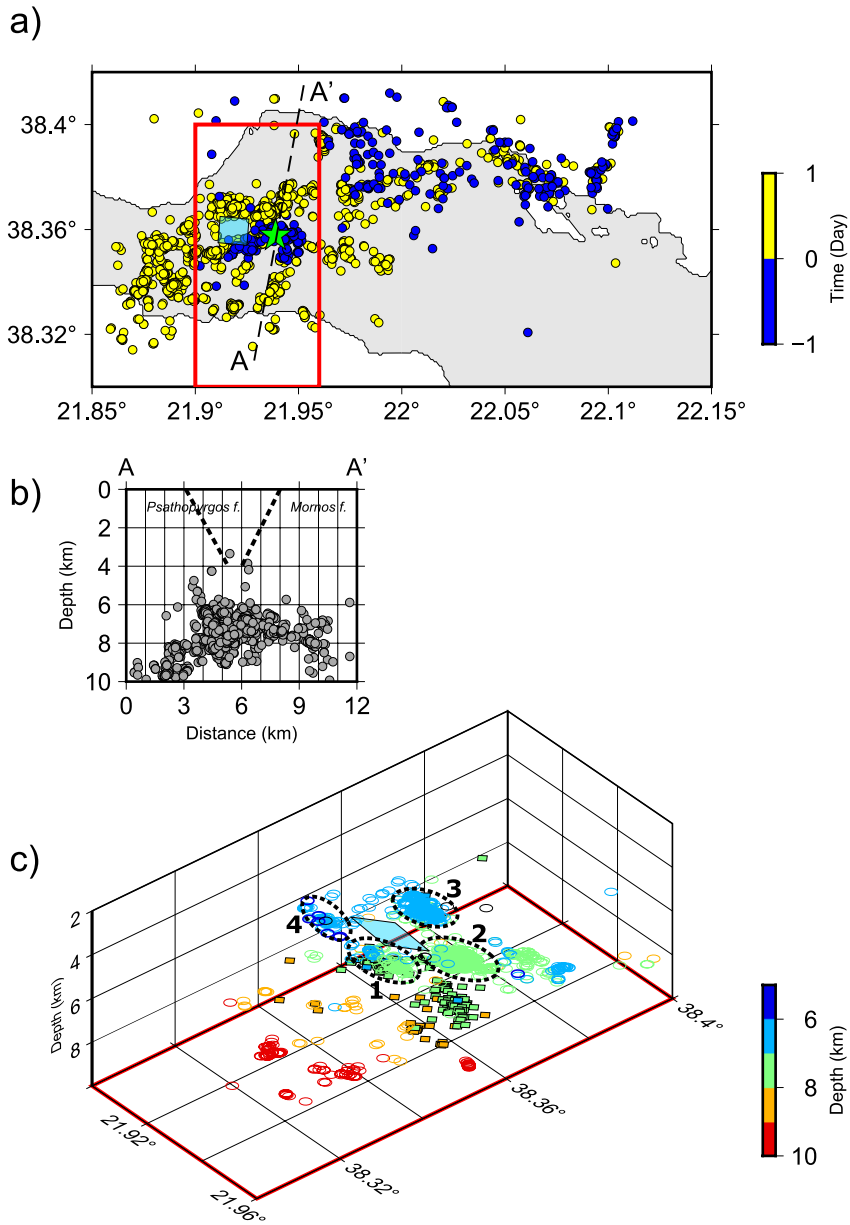

Figure 8. Relocated microseismicity ±24 h relative to origin time of the mainshock. (a) The western stop (limit) of the activity before the mainshock, and the nearby aftershock gap, are marked by a small transparent rectangle. The large red rectangle is detailed in panels b and (c) (b) Vertical cross-section along profile A-A'. (c) The gap in-between four clusters (1–4) is fitted with a fault segment that may correspond to the proposed deep Sub1 on the detachment layer. The events occurring 24 hours before and after the mainshock are shown with rectangles and circles, respectively, both color-coded with depth. Plotted here are 2554 relocated events of local magnitude 0.9–3.7. Since the mainshock could not be relocated, as explained in the main text, its position (the star) is shown here according to the absolute location of the present paper and Kaviris et al. (2021). The absolute locations can be compared only qualitatively with the relocated catalog. They differ on average by less than 1 km horizontally, with the standard deviation of ~800 m, and slightly more vertically, but the difference for the mainshock is larger, ~1 and ~2 km in the horizontal and vertical direction, respectively.

6. Discussion

6.1. Well-Revealed and Less Well-Revealed Features of the Feb17 Rupture Process

Here we briefly compile and compare some of the findings of the data analyses shown above. The Feb17 has been interpreted as an earthquake occurring on conjugate fault planes at different depths; this can be denoted as vertical (or down-dip) source segmentation. Compared to the fault segmentations recognizable on the Earth's

surface, such as bends, relays, or jogs, vertical segmentation is particularly challenging. As pointed out by Frietsch et al. (2021), distinguishing multiple subevents of down-dip segmented normal faults during moderate earthquakes is a difficult and understudied topic, important for seismic hazard assessments. Thus, the proposed two-segment faulting hypothesis must be critically examined as follows. The deep nucleation, Sub1, is well supported by the hypocentral location of the mainshock. It is partly supported by microearthquakes (foreshocks and aftershocks) situated in the detachment layer and surrounding the proposed Sub1 patch. The assumed low-angle north-dipping plane of Sub1 is consistent with the geometry of the detachment. The shallower depth and south-dipping fault plane of the major moment release, Sub2, is confirmed by independent evidence (CMT, GNSS, tide gauges). The bottom limit of the major slip patch Sub2 is situated above the detachment, but only a few shallow aftershocks are found close to the Sub2 patch (Figure 8b).

A link between the deep and shallower parts of the rupture is supported by the backprojection results but is debatable and its details remain unresolved. We have evidence from the EGF method that the entire rupture process could not evolve from depth to surface as a simple radially propagating rupture. The near-surface major slip patch of ∼5 × 5 km and its eastward directivity were explained in the EGF-based finite-extent source model, which required shallow nucleation – i.e., the 'second hypocenter'. If the 'second hypocenter' is merely a product of the applied methodology, an alternative explanation with a continuous rupture propagation from depth to surface (partly indicated by backprojection) is acceptable. In short, the mechanical forcing process between the early rupture (Sub1) and the shallow subevent (Sub2) remains unclear: it could either be an upward continuous rupture on unresolved fault fragments joining both large structures (consistent with the backprojection), or a dynamic/static triggering from one fault patch to the other, lying a few kilometers above (consistent with static Coulomb stress change and slip inversion).

6.2. Faults and Stress, Co-Existence of the Low- and High-Angle Faults

The dominant stress regime in the western Corinth Rift is extensional, characterized by the sub-vertical direction of maximum principal stress σ_1; plunge of $\sigma_1 \sim 80°$ (region 7 in Kapetanidis & Kassaras, 2019). As such, normal faulting at the proposed south-dipping shallow plane of Sub2, occurring at an angle of 30°–40° relative to σ_1, is compatible with optimally oriented ruptures and common friction values (Kanamori & Brodsky, 2004). Regarding the low-angle faulting on the deeper north-dipping plane, suggested as a nucleation phase Sub1, Rietbrock et al. (1996) proposed several explanations, such as low apparent friction or a non-vertical σ_1. The latter explanation would be compatible with observations from the Campotosto fault in the Apennines, where focal mechanisms indicated a decrease of the σ_1 plunge with depth (Figure 12 in Chiaraluce, 2012). Alternative explanations of low-angle normal faulting include reactivation below frictional lock-up, facilitated by elevated pore pressure (Collettini et al., 2011). This is an open question closely related to discussions of detachment rheology (Lambotte et al., 2014).

6.3. Deep and Shallow Fault Segments

A co-existence of high-angle normal faults and deeper sub-horizontal detachment shear zones similar to the one proposed here was typical for the 2016–2017 sequence of Central Italy (Waldhauser et al., 2021). Earthquakes on the detachment zone occurred there "in response" to the high-angle normal faults. Contrarily, during the 8-month-long preparatory phase of the 2016 August earthquake, the microseismic activity was occurring on the detachment and was then followed by an Mw 6.0 on steep normal faults (Vuan et al., 2017), as if the high-angle faults were "unzipped" by the deeper activity. It seems that Feb17 was a short-term analogy of this long-term process in Italy: The deep Sub1 (Mw 4.8) acted as a trigger for the shallow Sub2 (Mw 5.2), which was ready for rupturing due to stress load induced by the preceding activity of January 2021. In this sense, and also because we do not know the exact mechanical connection between Sub1 and Sub2, Sub1 could be considered as an immediate foreshock. In fact, a weak initial phase similar to Sub1 has already been detected in the Corinth rift for three Ms > 6 events of 1981 (Abercrombie et al., 1995).

The microseismic layer in which Sub1 nucleated was described in detail by Lambotte et al. (2014) and Duverger et al. (2015, 2018). These authors have clearly shown that this layer, into which the major normal faults are rooting, is composed of multiple small faults, and thus presents a structure fragmented at a few-kilometers scale. By simple geometric and energetic considerations, a large-scale efficient rupture propagation in such a medium

is not expected; see also Kame and Yamashita (1997). However, Sub1 was followed by the rupture of the larger and shallower fault segment Sub2. Dynamic modeling with adequate friction laws and prestress conditions, in particular in the shallow crust, might explain this complex cascading event, following an approach similar to Gallovič et al. (2020) for the Mw 6.8 Elazığ 2020 earthquake on the Eastern Anatolian fault. The deep nucleation (Sub1) and the major near-surface slip (Sub2) agree with current friction laws, according to which the velocity-strengthening shallow regions can rupture due to nucleation in a nearby deeper velocity-weakening region, while the shallow nucleation is inhibited (Kaneko et al., 2010). Velocity strengthening most probably could explain the paucity of shallow aftershocks (Figures 2 and 8). Few aftershocks (Ml $\leq$ 2.8) were also reported for the exceptionally shallow (0–2 km) Mw 4.9 Le Teil (France) earthquake (Delouis et al., 2021). At the Campotosto fault already mentioned, earthquake nucleation shallower than 6 km is also rare (Chiaraluce, 2012). Finally, almost no aftershock originated at the shallow slip depth of the 2014 Mw 6.0 South Napa (California) earthquake (Hardebeck & Shelly, 2016).

6.4. Association With a Geologic Fault

Is it possible to associate the proposed shallow faulting (Sub2) of the Feb17 mainshock with any known south-dipping, high-angle tectonic element in the gulf? For example, south-dipping faults on the northern coast have been discussed as possible causative faults of the 2010 Mw 5.3 and 5.2 Efpalio earthquakes (Elias, 2013; Sokos et al., 2012). The WGoC, as well as the whole gulf, is characterized by WNW-ESE normal faults. Nevertheless, there are also significant differences between the western and eastern parts of the gulf, e.g., the basement is significantly shallower in the western part, ∼1.0–1.5 km, compared to ∼3–4 km in the eastern part (Beckers, 2015; Beckers et al., 2015; Taylor et al., 2011). Furthermore, the polarity and faulting style also vary along the rift. According to Beckers (2015), the fault network is highly segmented in the western part, and the rift polarity changes over small distances, in agreement with the longer-term features reported by Moretti et al. (2003), emphasizing the activity of the south-dipping Trizonia fault system. Normal faulting and strike-slip motions seem to coexist in the western part of the gulf (e.g., Beckers, 2015; Sokos et al., 2012).

Focusing within ∼5 km of the Feb17 epicenter, the major normal faults are the north-dipping Psathopyrgos and Lambiri faults along the southern coast, and the south-dipping fault system of Marathias along the northern coast. Near the center of the basin, and closest to the epicenter, lies the western end of a significant offshore structure: the south-dipping Trizonia Fault System (TZFS), which includes the Trizonia and Mornos faults, shortly mentioned already in Figure 2, and discussed in detail here and in Figure 9. The most accurate and recent mapping of this offshore fault system is presented in Figure 6 of Beckers et al. (2015), who depicted the detailed segmentation of the Mornos fault system (referred to in their paper as the Managouli fault zone; MFZ). This fault system appears to be complex, exhibiting slight strike changes, as well as a horst separating the north-dipping and south-dipping normal faults, some of them also featuring strike-slip components. The main structure of the Mornos system is antithetic to the Psathopyrgos fault, and although it is well imaged by reflection seismic profiles, it is unclear whether it reaches the surface or remains blind (Beckers, 2015). The present-day Mornos delta subsidence is located at the footwall of this fault, suggesting that the Mornos fault is either inactive or not very active (Beckers, 2015; Elias, 2013; Parcharidis et al., 2013).

The major shallow subevent of the Feb17 mainshock (Sub2) is centered at 1–2 km south of the Mornos fault system, making the latter a good candidate for having ruptured during the event. Also, to the first order, their strike is similar. The source model appears shifted by a few kilometers westward of the mapped fault scarps F6 and F7 (Figure 9a), in an area where submarine slumps may blur or hide the MFZ expression according to Beckers et al. (2015, 2018). Therefore, we suggest that the earthquake source activated a mostly buried segment of the Mornos fault, on the southern slope of the horst (H4 in Figure 9), which may continue a few km westward. This rupture would thus represent the westernmost activation of the entire TZFS, which likely dies away under the Mornos delta edge. The alternative scenario, that of Sub2 occurring at shallow depth near the epicenter on the second nodal plane of the moment tensor (north-dip at a low angle of 30°–40°), is unlikely. It would indeed mean that the Psathopyrgos fault becomes listric at a very shallow depth, which is not supported by any geological studies.

A better understanding of the tectonic and mechanical significance of the unusually shallow Feb17 event is provided in a broader context of the geological history and development of the western rift of Corinth, as proposed by Ford et al. (2016). They showed that the TZFS, active between 0.8 and 0.4 Myr, in conjunction with

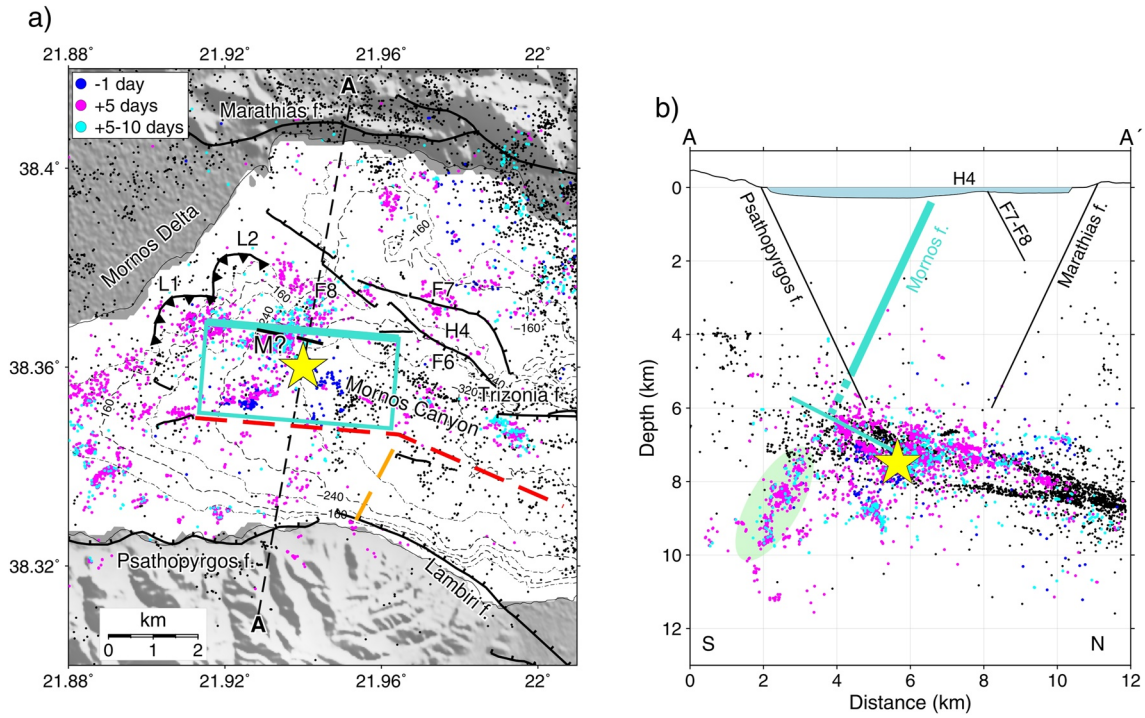

Figure 9. Conceptual seismo-tectonic sketch of the Feb17 earthquake. (a) Surface projection of the main slip area (Sub2) is shown by the rectangle, centered below the epicenter (star). The F6, F7, F8 faults, and horst H4 represent the western part of the Trizonia Fault System (TZFS), L1 and L2 are landslide head-scarps, M? is an uncertain fault; after Beckers et al. (2015). The yellow dashed line is the expected shallow intersection line between the Psathopyros and Lambiri faults. The red dashed line is an estimated intersection of the Psathopyrgos-Lambiri north dipping faults with the south-dipping fault system. The top (thicker) edge of Sub2 is located in the continuation of F6 and H4, and close to M?, likely depicting the Mornos fault buried in the slumps of the Mornos canyon. (b) Vertical cross-section along profile A-A' of the panel (a). It illustrates the geometrical/mechanical link of the involved local faults. The main rupture area (Sub2) is shown by a thick solid cyan line, centered above the hypocenter (star). The small subhorizontal cyan line passing near the hypocenter is the proposed initial low-angle source segment (Sub1). Small black circles depict the previous seismicity of 2000–2015 (Duverger et al., 2018), mapping the detachment layer. Microseismicity one day before and ten days after the mainshock is shown by color circles (see the color bar in panel a). Most of these microseismic events lie in the detachment layer. A small deeper group, shown by the cyan oval in panel b, indicates the likely root of the Mornos fault.

the north-dipping Helike-Lakka-Panakaikon fault system (situated to the south of our study area), was mostly deactivated by the northward shift of the rift. Since 0.4 Myr, the development of the Psathopyrgos and Marathias fault system has dominated. As a consequence, the Trizonia fault zone, being a major structure, is likely rooted in the detachment layer near the depth of 7–8 km, and so does also its westernmost segment, i.e., the south-dipping Mornos fault. The growing Psathopyrgos fault has likely cut through the Mornos fault at a depth of ~4–5 km, depending on the (uncertain) dip of the faults at depth (Figure 9b). A large tectonically cumulated slip of the Psathopyrgos fault is thus expected to have produced a major along-dip segmentation of the Mornos fault, rendering unlikely a large-scale seismic rupture (M6+) spanning the entire 0–8 km depth range. Our model of the Feb17 rupture, limited to the upper part of the Mornos fault, is thus consistent with this geometrical step inherited from the long history of the rift. However, this probably does not imply that its deepest part is deactivated.

A potentially important tectonic element indicated by the microseismicity pattern (Figure 8, Figure S7 in the Supporting Information S1) is highlighted by an oval in Figure 9b at depth 8–10 km, likely depicting a deep root of the Mornos fault – in agreement with the above-debated rift development. Indeed, geometrical extrapolation of the Mornos fault at depth matches the alignment of microseismic events between 8 and 10 km depth, within the uncertainties of the fault dip and relative focal locations. Note that the root at 8–10 km depth, seismically activated by the Feb 17 mainshock, was mostly seismically silent during the whole period 2000–2015 (Duverger et al., 2018), as seen by the paucity of small black circles in the oval of Figure 9b. Thus, the Mornos fault appears likely to be along-dip segmented into three pieces, being cut by the Psathopyrgos fault at 4–5 km depth and by the active detachment at 6–7 km, each of these three segments presenting a specific seismic signature, either due to different friction parameters, and/or due to a different stage in their loading cycle. The deep seismic root was activated in the form of microearthquakes, not by penetration of Sub1 or Sub2 beneath detachment. The root is

mainly formed by the foci of microearthquakes between 21.88°E and 21.96°E, and thus may correspond to the western termination of the Mornos fault under the Mornos delta; this, in turn, suggests that the TZFS extends westward far beyond the reported surface scarps. If confirmed in future studies, this effect may provide a hint for resolving the respective chronology of the development of the TZFS and the Psathopyrgos-Lambiri faults.

7. Conclusion and Perspectives

The 2020–2021 seismic crisis in the western Gulf of Corinth culminated with an Mw 5.3 earthquake on 17 February 2021 (Kaviris et al., 2021). We investigated this event in detail because of the interest it presents in terms of peculiar features as well as hazard – namely its proximity to the Psathopyrgos fault, a potential causative fault of a future Mw 6+ event that could affect the cities of Patras and Aigion.

Seismological, geodetic, and tide gauge data of the CRL network were used to infer the kinematics of the rupture process. The hypocenter was located at a depth of 8 ± 1.5 km. The CMT revealed a normal faulting mechanism and a shallow major moment release below the epicenter at depths ∼0–5 km. The GNSS and InSAR data estimated the main rupture depth at ∼2–3 km, the tide gauge data modeling provided ∼3–5 km, and seismic backprojection indicated ∼2–4 km. Thus, the combined data suggest a shallow moment release at a depth of ∼3 km with an uncertainty of 1–2 km. In such a geometrical configuration, the rupture could not have propagated from the hypocenter to the centroid along a single nodal plane.

We combine the available pieces of evidence into a two-segment rupture model, involving both conjugate nodal planes. Inversion of waveforms has been employed to jointly estimate the position, moment, and time-function of two-point sources (i.e., the subevent pairs). According to these models, the rupture likely nucleated at the hypocenter forming an Mw∼4.8 subevent on the low-angle, north-dipping detachment zone. Soon after (∼2 s) its initiation, the rupture process continued with an Mw∼5.2 subevent along a high-angle, south-dipping (dip ∼50–65°) normal fault segment, featuring eastward directivity (indicated by the EGF method) and releasing most of the seismic moment at the shallow depths. This mechanism is possible because the shallow normal fault was stress-loaded by the preceding activity of January 2021 and eventually triggered by the weak Mw∼4.8 initial rupture, on the detachment layer. The participation of both episodes of the mainshock, the deep and shallow one, was also confirmed by backprojection, but how exactly the rupture propagated from one to the other remains unknown.

The occurrence of a shallow M5+ event in such an offshore environment in the western Gulf of Corinth has not been instrumentally observed up to now. It can be interpreted as an activation of a south-dipping segment of the Mornos fault system, at the western tip of the south-dipping Trizonia fault system. In the existing literature, the Mornos fault has been investigated only recently, thanks to offshore seismic profiling, and seems to be one of the five major faults in the studied region. The shallow slip distribution is consistent with a likely geometrical barrier imposed by the leading Psathopyrgos fault, which has likely cut and segmented this south-dipping fault at a ∼4–5 km depth.

Further analysis of this event would be useful, namely a search for offshore surface ruptures in the sediments of the seafloor, which would require shallow water seismics, and/or imagery. A remaining notable question (to be answered by dynamic source modeling) is how the previously quiescent topmost layers of the rift enable the Feb17 mainshock to rupture, while, at the same time, not provoking any significant shallow aftershock activity there. More research is also needed on the respective roles of major faults in WGoC. For example, are the shallow parts of the Psathopyrgos fault at least partially releasing tectonic stress aseismically, as suggested by the short-lived transient observed in 2001 (Bernard et al., 2006), thus transferring stress to the antithetic shallow Mornos fault? Or is Mornos a mature fault that can be triggered by small stress perturbations from nearby swarms, without any decisive role of the Psathopyrgos fault?

Obviously, our study was challenged by the offshore character of the main event. In order to improve the permanent monitoring of the western part of the rift, in the framework of the Corinth Rift Near-Fault Observatory, the innovative research infrastructure within the European Plate Observing System (EPOS), one may investigate the feasibility and advantages of offshore monitoring with existing and emerging techniques. For instance, while DAS systems interrogating submarine optic cables would considerably help with detecting and locating shallow events (<5 km) beneath the gulf, the Brillouin Optical Time-Domain Reflectometer (BOTDR) system for long-term, repeatable strain measurements on dedicated submarine cables would allow detecting a continuous or transient slip in outcropping faults zones crossed by the fiber. Cabled OBS located

in the gulf could also greatly improve real-time monitoring of the rift, in particular with innovative optical seismometers (Bernard et al., 2019; Feron et al., 2020), which may considerably reduce the cost of their installation and maintenance. Such high-end equipment and techniques would meet societal needs for seismic and tsunami early warning.

In a broader perspective, the message our work conveys with respect to similar extensional structures elsewhere in the world is that a key role in their seismic hazard assessments can be played by marine geophysics investigations, searching for major fault structures analogous to the Mornos fault of this paper. Steep inner faults, synthetic/antithetic, together with onshore faults bounding the rift, all could in principle host future large earthquakes. To understand all processes taking part in a rift, mapping the seismicity is important but not sufficient. As we have shown, practically all seismicity in the Corinth Rift occurs in the form of microearthquakes on the detachment, and these are controlled by structures and rheology which differ from those of the steep normal faults likely hosting moderate-to-large earthquakes. Current conditions at the steep shallow faults are poorly known. The actual incohesive/cohesive characteristics of the involved fault rocks are controlled by a complex interplay between lithology, pressure/temperature conditions, mechanical/chemical processes, and fluids. Thus, in the Corinth rift or similar extensional structures elsewhere, we should anticipate future ruptures occurring on steep faults even in the presently seismically inactive crustal volume above the detachment, as demonstrated by the anomalously shallow Mw 5.3 earthquake highlighted in the study at hand.

Conflict of Interest

The authors declare no conflicts of interest relevant to this study.

Data Availability Statement

All data used in this study are publicly available. The new interactive seismic catalog of the National Observatory of Athens was searched at https://bbnet.gein.noa.gr/HL/databases/database. For the moment-tensor catalog of the University of Patras, see http://seismo.geology.upatras.gr/heliplots/amt/MTcat.html%23tableMT. The Global Centroid Moment Tensor Project database was searched using software www.globalcmt.org/CMTsearch.html. The Coulomb software (Toda et al., 2011) is available at https://pubs.usgs.gov/of/2011/1060/. For the most recent version of Isola software (Zahradník & Sokos, 2018), see http://geo.mff.cuni.cz/~jz/for_ISOLAnews/. Most figures were made using the Generic Mapping Tools (Wessel et al., 2019): https://www.generic-mapping-tools.org/. For the European Space Agency's Geohazard Exploitation Platform, see https://geohazards-tep.eu/. The EMODnet bathymetry was downloaded at https://portal.emodnet-bathymetry.eu and Navionics nautical charts at https://webapp.navionics.com/. Link to the Monastiraki "refined" grid used for the tsunami simulation, and the animated gif of the tsunami simulated on EMODNET "mother" grid: https://osf.io/7knup/?view_only=55141fc2e03643509b808d405ca7ac43. Link to AIGI tide gauge: Flanders Marine Institute (VLIZ); Intergovernmental Oceanographic Commission (IOC) (2022): Sea level station monitoring facility at https://www.ioc-sealevelmonitoring.org; https://doi.org/10.14284/482. Data from seismometers and accelerometers can be retrieved from ORFEUS (https://www.orfeus-eu.org/data/eida/nodes/), EIDA nodes at RESIF (Péquegnat et al., 2021), and NOA (Evangelidis et al., 2021). GNSS data and positioning solutions are available on the CRL portal (http://crlab.eu). Seismological data were acquired from stations installed and operated by the following institutions: (a) the CRL team (CL network, data hosted at RESIF, https://doi.org/10.15778/RESIF.CL), (b) the National and Kapodistrian University of Athens (NKUA) (HA network, data hosted at NOA, https://doi.org/10.7914/SN/HA), (c) the University of Patras (HP network, data hosted at NOA, https://doi.org/10.7914/SN/HP), which operates 11 stations jointly with Charles University, Prague, (d) the National Observatory of Athens (NOA) (HL network, data hosted at NOA, https://doi.org/10.7914/SN/HL), and (e) Institute of Engineering Seismology and Earthquake Engineering (ITSAK) (HI network, data hosted at NOA, https://doi.org/10.7914/SN/HI). Stations by the last four institutes are also part of the Hellenic Unified Seismological Network (HUSN), https://www.gein.noa.gr/en/networks-equipment/hellenic-unified-seismic-network-h-u-s-n/. GNSS observations were made with 13 stations (installed since 2002), 12 operated by the CRL team, and 1 by GI-NOA (Chousianitis et al., 2021; Ganas et al., 2008). The relocated automatic catalog (author: O. Lengliné) can be accessed at https://doi.org/10.5281/zenodo.5909709. All the links to data and resources cited above were last accessed in August 2022.

Acknowledgments
C.E., I.F., Z.R., and O.J.K. were supported by the Hellenic Foundation for Research and Innovation (H.F.R.I.) under the "First Call for HFRI Research Projects to support Faculty members and Researchers and the procurement of high-cost research equipment grant" (SIREN, Project Number: 910). O.J.K. was also supported by the internal NOA scholarship 'ROAR'. G.K. and N.V. acknowledge support from the Special Account for Research Grants of the National and Kapodistrian University of Athens (UoA – SARG). E.S and A.S acknowledge financial support from the HELPOS project, "Hellenic Plate Observing System" (MIS 5002697). We thank the personnel of CRLnet and HUSN who worked on the installation, operation, and maintenance of stations used in the current article. Constructive comments of the Editor (Rachel Abercrombie), the Associate Editor (Kate Huihsuan Chen), the reviewer Bogdan Enescu, and two anonymous reviewers improved the paper. The present work is dedicated to the memory of our late colleague Ioannis Kassaras who was among the founders of CRL and actively participated in the research in the region, even until his last days.

References

Abercrombie, R. E., Main, I. G., Douglas, A., & Burton, P. W. (1995). The nucleation and rupture process of the 1981 Gulf of Corinth earthquakes from deconvolved broad-band data. *Geophysical Journal International*, *120*, 393–405. https://doi.org/10.1111/j.1365-246X.1995.tb01827.x

Albini, P., Rovida, A., Scotti, O., & Lyon-Caen, H. (2017). Large eighteenth–nineteenth century earthquakes in western Gulf of Corinth with reappraised size and location. *Bulletin of the Seismological Society of America*, *107*(4), 1663–1687. https://doi.org/10.1785/0120160181

Aochi, H., & Kato, A. (2010). Dynamic rupture of crosscutting faults: A possible rupture process for the 2007 Mw 6.6 Niigata-ken Chuetsu-Oki earthquake. *Journal of Geophysical Research*, *115*, B05310. https://doi.org/10.1029/2009JB006556

Beckers, A. (2015). Late quaternary sedimentation in the western gulf of Corinth: Interplay between tectonic deformation, seismicity, and eustatic changes. (Doctoral dissertation). *Earth Sciences. Université Grenoble Alpes*.

Beckers, A., Hubert-Ferrari, A., Beck, C., Bodeux, S., Tripsanas, E., Sakellariou, D., & De Batist, M. (2015). Active faulting at the western tip of the Gulf of Corinth, Greece, from high-resolution seismic data. *Marine Geology*, *360*, 55–69. https://doi.org/10.1016/j.margeo.2014.12.003

Beckers, A., Hubert-Ferrari, A., Beck, C., Papatheodorou, G., Batist, M., Sakellariou, D., et al. (2018). Characteristics and frequency of large submarine landslides at the western tip of the Gulf of Corinth. *Natural Hazards and Earth System Sciences*, *18*, 1411–1425. https://doi.org/10.5194/nhess-18-1411-2018

Bell, R., McNeill, L., Bull, J., Henstock, T., Collier, R., & Leeder, R. (2009). Fault architecture, basin structure and evolution of the Gulf of Corinth Rift, central Greece. *Basin Research*, *21*, 824–855. https://doi.org/10.1111/j.1365-2117.2009.00401.x

Bell, R. E., McNeill, L. C., Bull, J. M., & Henstock, T. J. (2008). Evolution of the offshore western Gulf of Corinth. *Geological Society of America Bulletin*, *120*(1–2), 156–178. https://doi.org/10.1130/B26212.1

Bernard, P., Briole, P., Meyer, B., Gomez, J., Tiberi, C., Berge, C., et al. (1997). The M_s=6.2, June 15, 1995 Aigion earthquake (Greece): Evidence for low-angle normal faulting in the Corinth Rift. *Journal of Seismology*, *1*, 131–150. https://doi.org/10.1023/A:1009795618839

Bernard, P., Feron, R., Plantier, G., Nercessian, A., Couteau, J., Sourice, A., et al. (2019). Onland and offshore extrinsic Fabry–Pérot optical seismometer at the end of a long fiber. *Seismological Research Letters*, *90*(6), 2205–2216. https://doi.org/10.1785/0220190049

Bernard, P., Lyon-Caen, H., Briole, P., Deschamps, A., Boudin, F., Makropoulos, K., et al. (2006). Seismicity, deformation and seismic hazard in the western rift of Corinth: New insights from the Corinth Rift laboratory (CRL). *Tectonophysics*, *426*, 7–30. https://doi.org/10.1016/j.tecto.2006.02.012

Bernard, P., & Zollo, A. (1989). The Irpinia (Italy) 1980 earthquake: Detailed analysis of a complex normal faulting. *Journal of Geophysical Research*, *94*(B2), 1631–1647. https://doi.org/10.1029/JB094iB02p01631

Boiselet, A. (2014). Cycle sismique et aléa sismique d'un réseau de failles actives: Le cas du rift de Corinthe (Grèce). (Doctoral dissertation. in French).

Bourouis, S., & Cornet, F. H. (2009). Microseismic activity and fluid fault interactions: Some results from the Corinth Rift Laboratory (CRL), Greece. *Geophysical Journal International*, *178*, 561–580. https://doi.org/10.1111/j.1365-246X.2009.04148.x

Braunmiller, J., & Nábělek, J. (1996). Geometry of continental normal faults: Seismological constraints. *Journal of Geophysical Research*, *101*(B2), 3045–3052. https://doi.org/10.1029/95JB02882

Briole, P. (2017). Modelling of earthquake slip by inversion of GPS and InSAR data assuming homogenous elastic medium (Version 1). *ZENODO*. https://doi.org/10.5281/ZENODO.1098399

Briole, P., De Natale, G., Gaulon, R., Pingue, F., & Scarpa, R. (1986). Inversion of geodetic data and seismicity associated with the Friuli earthquake sequence (1976–1977). *Annales Geophysicae*, *4*(B4), 481–492.

Briole, P., Ganas, A., Elias, P., & Dimitrov, D. (2021). The GPS velocity field of the Aegean. New observations, contribution of the earthquakes, crustal blocks model. *Geophysical Journal International*, *226*(1), 468–492. https://doi.org/10.1093/gji/ggab089

Calderoni, G., Rovelli, A., & Di Giovambattista, R. (2017). Rupture directivity of the strongest 2016–2017 central Italy earthquakes. *Journal of Geophysical Research: Solid Earth*, *122*, 9118–9131. https://doi.org/10.1002/2017JB014118

Champenois, J., Baize, S., Vallee, M., Jomard, H., Alvarado, A. P., Espin, P., et al. (2017). Evidences of surface rupture associated with a low-magnitude (Mw5.0) shallow earthquake in the Ecuadorian Andes. *Journal of Geophysical Research: Solid Earth*, *122*, 8446–8458. https://doi.org/10.1002/2017JB013928

Chen, C. W., & Zebker, H. A. (2002). Phase unwrapping for large SAR interferograms: Statistical segmentation and generalized network models. *IEEE Transactions on Geoscience and Remote Sensing*, *40*, 1709–1719. https://doi.org/10.1109/tgrs.2002.802453

Chéry, J. (2001). Core complex mechanics: From the Gulf of Corinth to the Snake Range. *Geology*, *29*, 439–442. https://doi.org/10.1130/0091-7613(2001)029<0439:CCMFTG>2.0.CO;2

Chiaraluce, L. (2012). Unravelling the complexity of Apenninic extensional fault systems: A review of the 2009 L'Aquila earthquake (central Apennines, Italy). *Journal of Structural Geology*, *42*, 2–18. https://doi.org/10.1016/j.jsg.2012.06.007

Chousianitis, K., Papanikolaou, X., Drakatos, G., & Tselentis, G.-A. (2021). NOANET: A continuously operating GNSS network for solid-Earth sciences in Greece. *Seismological Research Letters*, *92*(3), 2050–2064. https://doi.org/10.1785/0220200340

Collettini, C., Niemeijer, A., Viti, C., Smith, S. A. F., & Marone, C. (2011). Fault structure, frictional properties and mixed-mode fault slip behavior. *Earth and Planetary Science Letters*, *311*, 316–327. https://doi.org/10.1016/j.epsl.2011.09.020

Cowie, P. A., Phillips, R. J., Roberts, G. P., McCaffrey, K., Zijerveld, L. J. J., Gregory, L. C., et al. (2017). Orogen-scale uplift in the central Italian Apennines drives episodic behaviour of earthquake faults. *Scientific Reports*, *7*, 44858. https://doi.org/10.1038/srep44858

Cowie, P. A., Scholz, C. H., Roberts, G. P., Faure Walker, J. P., & Steer, P. (2013). Viscous roots of seismogenic faults revealed by geologic slip rate variations. *Nature Geoscience*, *6*, 1036–1040. https://doi.org/10.1038/ngeo1991

Craig, T. J., Jackson, J. A., Priestley, K., & McKenzie, D. (2011). Earthquake distribution patterns in Africa: Their relationship to variations in lithospheric and geological structure, and their rheological implications. *Geophysical Journal International*, *185*, 403–434. https://doi.org/10.1111/j.1365-246X.2011.04950.x

Dalla Via, G., Crosetto, M., & Crippa, B. (2012). Resolving vertical and east-west horizontal motion from differential interferometric synthetic aperture radar: The L'Aquila earthquake. *Journal of Geophysical Research*, *117*, B02310. https://doi.org/10.1029/2011JB008689

De Barros, L., Cappa, F., Deschamps, A., & Dublanchet, P. (2020). Imbricated aseismic slip and fluid diffusion drive a seismic swarm in the Corinth Gulf, Greece. *Geophysical Research Letters*, *47*(9), e2020GL087142. https://doi.org/10.1029/2020GL087142

Delouis, B., Oral, E., Menager, M., Ampuero, J.-P., Trilla, A. G., Régnier, M., & Deschamps, A. (2021). Constraining the point source parameters of the 11 November 2019 Mw 4.9 Le Teil earthquake using multiple relocation approaches, first motion and full waveform inversions. *Comptes Rendus Geoscience*, *353*(S1), 493–516. https://comptes-rendus.academie-sciences.fr/geoscience/articles/10.5802/crgeos.78/

Doglioni, C., Barba, S., Carminati, E., & Riguzzi, F. (2015). Fault on-off versus strain rate and earthquakes energy. *Geoscience Frontiers*, *6*, 265–276. https://doi.org/10.1016/j.gsf.2013.12.007

Dreger, D. (1994). Empirical Green's function study of the January 17, 1994 Northridge, California earthquake. *Geophysical Research Letters*, *21*, 2633–2636. https://doi.org/10.1029/94GL02661

Duverger, C., Godano, M., Bernard, P., Lyon-Caen, H., & Lambotte, S. (2015). The 2003-2004 seismic swarm in the western Corinth rift: Evidence for a multiscale pore pressure diffusion process along a permeable fault system. *Geophysical Research Letters*, *42*, 7374–7382. https://doi.org/10.1002/2015GL065298

Duverger, C., Lambotte, S., Bernard, P., Lyon-Caen, H., Deschamps, A., & Nercessian, A. (2018). Dynamics of microseismicity and its relationship with the active structures in the western Corinth Rift (Greece). *Geophysical Journal International*, *215*, 196–221. https://doi.org/10.1093/gji/ggy264

Ebinger, C. J., Oliva, S. J., Pham, T.-Q., Peterson, K., Chindandali, P., Illsley-Kemp, F., et al. (2019). Kinematics of active deformation in the Malawi rift and Rungwe Volcanic Province, Africa. *Geochemistry, Geophysics, Geosystems*, *20*, 3928–3951. https://doi.org/10.1029/2019GC008354

Elias, P. (2013). Ground deformation observed in the western Corinth rift (Greece) by means of SAR interferometry. *Doctoral dissertation). Ecole Normale Supérieure (Paris) and University of Patras*. http://www.theses.fr/2013ENSUBS18

Elias, P., & Briole, P. (2018). Ground deformations in the Corinth rift, Greece, investigated through the means of SAR multitemporal interferometry. *Geochemistry, Geophysics, Geosystems*, *19*, 4836–4857. https://doi.org/10.1029/2018GC007574

Ellsworth, W. L., Giardini, D., Townend, J., Ge, S., & Shimamoto, T. (2019). Triggering of the Pohang, Korea, earthquake (Mw 5.5) by enhanced geothermal system stimulation. *Seismological Research Letters*, *90*(5), 1844–1858. https://doi.org/10.1785/0220190102

Evangelidis, C. P. (2015). Imaging supershear rupture for the 2014 Mw6.9 Northern Aegean earthquake by backprojection of strong motion waveforms. *Geophysical Research Letters*, *42*(2), 307–315. https://doi.org/10.1002/2014GL062513

Evangelidis, C. P., Triantafyllis, N., Samios, M., Boukouras, K., Kontakos, K., Ktenidou, O.-J., et al. (2021). Seismic waveform data from Greece and Cyprus: Integration, archival, and open access. *Seismological Research Letters*, *92*(3), 1672–1684. https://doi.org/10.1785/0220200408

Feron, R., Bernard, P., Feuilloy, M., Ménard, P., Nercessian, A., Deroussi, S., et al. (2020). First optical seismometer at the top of La Soufrière volcano, Guadeloupe, *91*, 2448–2457.

Figueiredo, P. M., Hill, J. S., Merschat, A. J., Scheip, C. M., Stewart, K. G., Owen, L. A., et al. (2022). The Mw 5.1, 9 August 2020, Sparta earthquake, North Carolina: The first documented seismic surface rupture in the Eastern United States. *Geological Society of America Today*, *32*(3–4), 4–11. https://doi.org/10.1130/GSATG517A.1

Ford, M., Hemelsdaël, R., Mancini, M., & Palyvos, N. (2016). Rift migration and lateral propagation: Evolution of normal faults and sediment-routing systems of the western Corinth Rift (Greece). *Geological Society, London, Special Publications*, *439*, 131–168. https://doi.org/10.1144/SP439.15

Frietsch, M., Ferreira, A. M. G., & Funning, G. J. (2021). Data-driven two-fault modeling of the Mw 6.0 2008 Wells, Nevada earthquake suggests a listric fault rupture. *Journal of Geophysical Research: Solid Earth*, *126*, e2020JB020263. https://doi.org/10.1029/2020JB020263

Gallovič, F., Zahradník, J., Plicka, V., Sokos, E., Evangelidis, C., Fountoulakis, I., & Turhan, F. (2020). Complex rupture dynamics on an immature fault during the 2020 Mw 6.8 Elazığ earthquake, Turkey. *Communications Earth & Environment*, *1*, 40. https://doi.org/10.1038/s43247-020-00038-x

Ganas, A., Drakatos, G., Rontogianni, S., Tsimi, C., Petrou, P., Papanikolaou, M., et al. (2008). NOANET: The new permanent GPS network for Geodynamics in Greece. *Geophysical Research Abstracts*, *10*, EGU2008-A-04380.

Glimsdal, S., Pedersen, G. K., Harbitz, C. B., & Løvholt, F. (2013). Dispersion of tsunamis: Does it really matter? *Natural Hazards and Earth System Sciences*, *13*, 1507–1526. https://doi.org/10.5194/nhess-13-1507-2013

Grünthal, G., & Wahlström, R. (2012). The European-Mediterranean Earthquake Catalogue (EMEC) for the last millennium. *Journal of Seismology*, *16*, 535–570. https://doi.org/10.1007/s10950-012-9302-y

Hallo, M., Asano, K., & Gallovič, F. (2017). Bayesian inference and interpretation of centroid moment tensors of the 2016 Kumamoto earthquake sequence, Kyushu, Japan. *Earth Planets and Space*, *69*, 134. https://doi.org/10.1186/s40623-017-0721-4

Hallo, M., & Gallovič, F. (2016). Fast and cheap approximation of Green function uncertainty for waveform-based earthquake source inversions. *Geophysical Journal International*, *207*, 1012–1029. https://doi.org/10.1093/gji/ggw320

Hallo, M., Opršal, I., Asano, K., & Gallovič, F. (2019). Seismotectonics of the 2018 northern Osaka M6.1 earthquake and its aftershocks: Joint movements on strike-slip and reverse faults in inland Japan. *Earth Planets and Space*, *71*, 34. https://doi.org/10.1186/s40623-019-1016-8

Hardebeck, J., & Shelly, D. (2016). Aftershocks of the 2014 South Napa, California, earthquake: Complex faulting on secondary faults. *Bulletin of the Seismological Society of America*, *106*, 1100–1109. https://doi.org/10.1785/0120150169

Heinrich, P., Jamelot, A., Cauquis, A., & Gailler, A. (2021). Taitoko, an advanced code for tsunami propagation, developed at the French Tsunami Warning Centers. *European Journal of Mechanics - B: Fluids*, *88*, 72–88. https://doi.org/10.1016/j.euromechflu.2021.03.001

Ide, S., Baltay, A., & Beroza, G. C. (2011). Shallow dynamic overshoot and energetic deep rupture in the 2011 Mw 9.0 Tohoku-Oki earthquake. *Science*, *332*(6036), 1426–1429. https://doi.org/10.1126/science.1207020

Kame, N., & Yamashita, T. (1997). Dynamic nucleation process of shallow earthquake faulting in a fault zone. *Geophysical Journal International*, *128*(1), 204–216. https://doi.org/10.1111/j.1365-246x.1997.tb04081.x

Kanamori, H., & Brodsky, E. E. (2004). The physics of earthquakes. *Reports on Progress in Physics*, *67*, 1429–1496. https://doi.org/10.1088/0034-4885/67/8/R03

Kaneko, Y., Avouac, J. P., & Lapusta, N. (2010). Towards inferring earthquake patterns from geodetic observations of interseismic coupling. *Nature Geoscience*, *3*, 363–369. https://doi.org/10.1038/ngeo843

Kaneko, Y., & Fialko, Y. (2011). Shallow slip deficit due to large strike-slip earthquakes in dynamic rupture simulations with elasto-plastic off-fault response. *Geophysical Journal International*, *186*, 1389–1403. https://doi.org/10.1111/j.1365-246X.2011.05117.x

Kao, H., & Shan, S.-J. (2004). The Source-Scanning Algorithm: Mapping the distribution of seismic sources in time and space. *Geophysical Journal International*, *157*(2), 589–594. https://doi.org/10.1111/j.1365-246X.2004.02276.x

Kao, H., & Shan, S.-J. (2007). Rapid identification of earthquake rupture plane using Source-Scanning Algorithm. *Geophysical Journal International*, *168*(3), 1011–1020. https://doi.org/10.1111/j.1365-246X.2006.03271.x

Kapetanidis, V. (2017). Spatiotemporal Patterns of Microseismicity for the Identification of Active Fault Structures using Seismic Waveform Cross-Correlation and Double-Difference Relocation. *Doctoral dissertation). Department of Geophysics-Geothermics, Faculty of Geology and Geoenvironment, National and Kapodistrian University of Athens*. https://doi.org/10.12681/eadd/40717

Kapetanidis, V., Deschamps, A., Papadimitriou, P., Matrullo, E., Karakonstantis, A., Bozionelos, G., et al. (2015). The 2013 earthquake swarm in Helike, Greece: Seismic activity at the root of old normal faults. *Geophysical Journal International*, *202*, 2044–2073. https://doi.org/10.1093/gji/ggv249

Kapetanidis, V., & Kassaras, I. (2019). Contemporary crustal stress of the Greek region deduced from earthquake focal mechanisms. *Journal of Geodynamics*, *123*, 55–82. https://doi.org/10.1016/j.jog.2018.11.004

Kapetanidis, V., & Papadimitriou, P. (2011). Estimation of arrival-times in intense seismic sequences using a Master-Events methodology based on waveform similarity. *Geophysical Journal International*, *187*(2), 889–917. https://doi.org/10.1111/j.1365-246X.2011.05178.x

Kassaras, I., Kapetanidis, V., & Karakonstantis, A. (2016). On the spatial distribution of seismicity and the 3D tectonic stress field in western Greece. *Physics and Chemistry of the Earth, Parts A/B/C*, *95*, 50–72. https://doi.org/10.1016/j.pce.2016.03.012

Kato, A., Kurashimo, E., Igarashi, T., Sakai, S., Iidaka, T., Shinohara, M., et al. (2009). Reactivation of ancient rift systems triggers devastating intraplate earthquakes. *Geophysical Research Letters*, *36*, L05301. https://doi.org/10.1029/2008GL036450

Kaviris, G., Elias, P., Kapetanidis, V., Serpetsidaki, A., Karakonstantis, A., Plicka, V., et al. (2021). The western Gulf of Corinth (Greece) 2020–2021 seismic crisis and cascading events: First results from the Corinth Rift Laboratory Network. *The Seismic Record*, *1*(2), 85–95. https://doi.org/10.1785/0320210021

Kaviris, G., Millas, C., Spingos, I., Kapetanidis, V., Fountoulakis, I., Papadimitriou, P., et al. (2018). Observations of shear-wave splitting parameters in the Western Gulf of Corinth focusing on the 2014 Mw=5.0 earthquake. *Physics of the Earth and Planetary Interiors*, *282*, 60–76. https://doi.org/10.1016/j.pepi.2018.07.005

Kaviris, G., Spingos, I., Kapetanidis, V., Papadimitriou, P., Voulgaris, N., & Makropoulos, K. (2017). Upper crust seismic anisotropy study and temporal variations of shear-wave splitting parameters in the Western Gulf of Corinth (Greece) during 2013. *Physics of the Earth and Planetary Interiors*, *269*, 148–164. https://doi.org/10.1016/j.pepi.2017.06.006

Kiratzi, A. (2018). The 12 June 2017 Mw 6.3 Lesvos Island (Aegean Sea) earthquake: Slip model and directivity estimated with finite-fault inversion. *Tectonophysics*, *724*, 1–10. https://doi.org/10.1016/j.tecto.2018.01.003

Kissling, E., Kradolfer, U., & Maurer, H. (1995). *Program VELEST user's guide - short introduction*. Institute of Geophysics. https://seg.ethz.ch/software/velest.html

Kostka, F., Zahradník, J., Sokos, E., & Gallovič, F. (2022). Assessing the role of selected constraints in Bayesian dynamic source inversion: Application to the 2017 M w 6.3 Lesvos earthquake. *Geophysical Journal International*, *228*(1), 711–727. https://doi.org/10.1093/gji/ggab359

Lambotte, S., Lyon-Caen, H., Bernard, P., Deschamps, A., Patau, G., Nercessian, A., et al. (2014). Reassessment of the rifting process in the Western Corinth Rift from relocated seismicity. *Geophysical Journal International*, *197*, 1822–1844. https://doi.org/10.1093/gji/ggu096

Lavayssière, A., Drooff, C., Ebinger, C., Gallacher, R., Illsley-Kemp, F., Oliva, S. J., & Keir, D. (2019). Depth extent and kinematics of faulting in the southern Tanganyika rift, Africa. *Tectonics*, *38*, 842–862. https://doi.org/10.1029/2018TC005379

Lawson, C. L., & Hanson, R. J. (1974). *Solving least squares Problems*. Prentice-Hall.

Lecomte, E., Le Pourhiet, L., & Lacombe, O. (2012). Mechanical basis for slip along low-angle normal faults. *Geophysical Research Letters*, *39*, L03307. https://doi.org/10.1029/2011GL050756

Lengliné, O., Duputel, Z., & Ferrazzini, V. (2016). Uncovering the hidden signature of a magmatic recharge at Piton de la Fournaise volcano using small earthquakes. *Geophysical Research Letters*, *43*(9), 4255–4262. https://doi.org/10.1002/2016GL068383

Le Pourhiet, L., Burov, E., & Moretti, I. (2003). Initial crustal thickness geometry controls on the extension in a back arc domain: Case of the Gulf of Corinth. *Tectonics*, *22*, 1032–n. https://doi.org/10.1029/2002TC001433

Lin, J., & Stein, R. S. (2004). Stress triggering in thrust and subduction earthquakes and stress interaction between the southern San Andreas and nearby thrust and strike-slip faults. *Journal of Geophysical Research*, *109*(B2), 589. https://doi.org/10.1029/2003JB002607

Liu, J., & Zahradník, J. (2020). The 2019 MW 5.7 Changning earthquake, Sichuan Basin, China: A shallow doublet with different faulting styles. *Geophysical Research Letters*, *47*, e2019GL085408. https://doi.org/10.1029/2019GL085408

Lomax, A., Zollo, A., Capuano, P., & Virieux, J. (2001). Precise, absolute earthquake location under Somma-Vesuvius volcano using a new three-dimensional velocity model. *Geophysical Journal International*, *146*(2), 313–331. https://doi.org/10.1046/j.0956-540X.2001.01444.x

López-Comino, J. A., Stich, D., Morales, J., & Ferreira, A. M. G. (2016). Resolution of rupture directivity in weak events: 1-D versus 2-D source parameterizations for the 2011, Mw 4.6 and 5.2 Lorca earthquakes, Spain. *Journal of Geophysical Research: Solid Earth*, *121*, 6608–6626. https://doi.org/10.1002/2016JB013227

Makropoulos, K., Kaviris, G., & Kouskouna, V. (2012). An updated and extended earthquake catalogue for Greece and adjacent areas since 1900. *Natural Hazards and Earth System Sciences*, *12*, 1425–1430. https://doi.org/10.5194/nhess-12-1425-2012

Mesimeri, M., Ganas, A., & Pankow, K. L. (2022). Multisegment ruptures and Vp/Vs variations during the 2020–2021 seismic crisis in western Corinth Gulf, Greece. *Geophysical Journal International*, *230*, 334–348. https://doi.org/10.1093/gji/ggac081

Mesimeri, M., Karakostas, V., Papadimitriou, E., Schaff, D., & Tsaklidis, G. (2016). Spatio-temporal properties and evolution of the 2013 Aigion earthquake swarm (Corinth Gulf, Greece). *Journal of Seismology*, *20*(2), 595–614. https://doi.org/10.1007/s10950-015-9546-4

Moretti, I., Sakellariou, D., Lykousis, V., & Micarelli, L. (2003). The Gulf of Corinth: An active half graben? *Journal of Geodynamics*, *36*(1–2), 323–340. https://doi.org/10.1016/S0264-3707(03)00053-X

Mori, J., & Hartzell, S. (1990). Source inversion of the 1988 Upland, California, earthquake: Determination of a fault plane for a small event. *Bulletin of the Seismological Society of America*, *80*(3), 507–518. https://doi.org/10.1785/BSSA0800030507

Mouslopoulou, V., Hristopulos, D. T., Nicol, A., Walsh, J. J., & Bannister, S. (2013). The importance of microearthquakes in crustal extension of an active rift: A case study from New Zealand. *Journal of Geophysical Research: Solid Earth*, *118*, 1556–1568. https://doi.org/10.1002/jgrb.50062

Okada, Y. (1985). Surface deformation due to shear and tensile faults in a half-space. *Bulletin of the Seismological Society of America*, *75*, 1135–1154. https://doi.org/10.1785/bssa0750041135

Oner, Z., & Dilek, Y. (2011). Supradetachment basin evolution during continental extension: The Aegean province of western Anatolia, Turkey. *Geological Society of America Bulletin*, *123*(11–12), 2115–2141. https://doi.org/10.1130/B30468.1

Pacchiani, F., & Lyon-Caen, H. (2010). Geometry and spatio-temporal evolution of the 2001 Agios Ioanis earthquake swarm (Corinth Rift, Greece). *Geophysical Journal International*, *180*, 59–72. https://doi.org/10.1111/j.1365-246X.2009.04409.x

Pacor, F., Gallovič, F., Puglia, R., Luzi, L., & D'Amico, M. (2016). Diminishing high-frequency directivity due to a source effect: Empirical evidence from small earthquakes in the Abruzzo region, Italy. *Geophysical Research Letters*, *43*, 5000–5008. https://doi.org/10.1002/2016GL068546

Palyvos, N., Pantosti, D., DeMartini, P. M., Lemeille, F., Sorel, D., & Pavlopoulos, K. (2005). The Aigion-Neos Erineos normal fault system (Western Corinth Gulf Rift, Greece): Geomorphological signature, recent earthquake history and evolution. *Journal of Geophysical Research*, *110*, B09302. https://doi.org/10.1029/2004JB003165

Palyvos, N., Pantosti, D., Stamatopoulos, L., & De Martini, P. M. (2007). Geomorphological reconnaissance of the Psathopyrgos and Rion-Patras fault zones (Achaia, NW Peloponnesus). *Bulletin of the Geological Society of Greece*, *40*, 1586–1598. https://doi.org/10.12681/bgsg.17063

Parcharidis, I., Kourkouli, P., Karymbalis, E., Foumelis, M., & Karathanassi, V. (2013). Time series synthetic aperture radar interferometry for ground deformation monitoring over a small scale tectonically active deltaic environment (Mornos, Central Greece). *Journal of Coastal Research*, *29*, 325–338. https://doi.org/10.2112/JCOASTRES-D-11-00106.1

Péquegnat, C., Schaeffer, J., Satriano, C., Pedersen, H., Touvier, J., Saurel, J.-M., et al. (2021). RÉSIF-SI: A Distributed Information System for French Seismological Data. *Seismological Research Letters*, *92*(3), 1832–1853. https://doi.org/10.1785/0220200392

Picozzi, M., Bindi, D., Festa, G., Cotton, F., Scala, A., & D'Agostino, N. (2022). Spatiotemporal evolution of microseismicity seismic source properties at the Irpinia Near-Fault Observatory, Southern Italy. *Bulletin of the Seismological Society of America*, *112*(1), 226–242. https://doi.org/10.1785/0120210064

Pino, N., & Mazza, S. (2000). The Umbria-Marche (central Italy) earthquakes: Relation between rupture directivity and sequence evolution for the Mw > 5 shocks. *Journal of Seismology*, *4*, 451–461. https://doi.org/10.1023/A:1026579300852

Rietbrock, A., Tiberi, C., Sherbaum, F., & Lyon-Caen, H. (1996). Seismic slip on a low angle normal fault in the Gulf of Corinth: Evidence from high resolution cluster analysis of microearthquakes. *Geophysical Research Letters*, *23*, 1817–1820. https://doi.org/10.1029/96GL01257

Rigo, A., Lyon-Caen, H., Armijo, R., Deschamps, A., Hatzfeld, D., Makropoulos, K., et al. (1996). A microseismic study in the western part of the gulf of Corinth (Greece): Implication for large-scale normal faulting mechanisms. *Geophysical Journal International*, *126*, 663–688. https://doi.org/10.1111/j.1365-246X.1996.tb04697.x

Serpetsidaki, A., Sokos, E., & Paraskevopoulos, P. (2021). *A revised moment tensor catalog for Western Greece*. Abstract book of the 37th General Assembly of the European Seismological Commission. ESC2021-S27-374.

Serpetsidaki, A., Sokos, E., & Tselentis, A. (2016). A ten year moment tensor database for Western Greece. *Physics and Chemistry of the Earth, Parts A/B/C*, *95*, 2–9. https://doi.org/10.1016/j.pce.2016.04.007

Sokos, E., Gallovič, F., Evangelidis, C. P., Serpetsidaki, A., Plicka, V., Kostelecký, J., & Zahradník, J. (2020). The 2018 Mw 6.8 Zakynthos, Greece, earthquake: Dominant strike-slip faulting near subducting slab. *Seismological Research Letters*, *91*, 721–732. https://doi.org/10.1785/0220190169

Sokos, E., & Zahradník, J. (2013). Evaluating centroid-moment-tensor uncertainty in the new version of ISOLA software. *Seismological Research Letters*, *84*, 656–665. https://doi.org/10.1785/0220130002

Sokos, E., Zahradník, J., Kiratzi, A., Janský, J., Gallovič, F., Novotný, O., et al. (2012). The January 2010 Efpalio earthquake sequence in the western Corinth Gulf (Greece). *Tectonophysics*, *530–531*, 299–309. https://doi.org/10.1016/j.tecto.2012.01.005

Stucchi, M., Rovida, A., Gomez Capera, A. A., Alexandre, P., Camelbeeck, T., Demircioglu, M. B., et al. (2013). The SHARE European Earthquake Catalogue (SHEEC) 1000-1899. *Journal of Seismology*, *17*, 523–544. https://doi.org/10.1007/s10950-012-9335-2

Styron, R. H., & Hetland, E. A. (2014). Estimated likelihood of observing a large earthquake on a continental low-angle normal fault and implications for low-angle normal fault activity. *Geophysical Research Letters*, *41*, 2342–2350. https://doi.org/10.1002/2014GL059335

Taylor, B., Weiss, J. R., Goodliffe, A. M., Sachpazi, M., Laigle, M., & Hirn, A. (2011). The structures, stratigraphy and evolution of the Gulf of Corinth rift, Greece. *Geophysical Journal International*, *185*, 1189–1219. https://doi.org/10.1111/j.1365-246X.2011.05014.x

Tinti, E., Casarotti, E., Ulrich, T., Taufiqurrahman, T., Li, D., & Gabriel, A.-A. (2021). Constraining families of dynamic models using geological, geodetic and strong ground motion data: The Mw 6.5, October 30th, 2016, Norcia earthquake, Italy. *Earth and Planetary Science Letters*, *576*, 117237. https://doi.org/10.1016/j.epsl.2021.117237

Toda, S., Stein, R. S., Richards-Dinger, K., & Bozkurt, S. B. (2005). Forecasting the evolution of seismicity in southern California: Animations built on earthquake stress transfer. *Journal of Geophysical Research*, *110*, B05S16. https://doi.org/10.1029/2004JB003415

Toda, S., Stein, R. S., Sevilgen, V., & Lin, J. (2011). Coulomb 3.3 Graphic-rich deformation and stress-change software for earthquake, tectonic, and volcano research and teaching — User guide. *U.S. Geological Survey Open-File Report 2011–*, *1060*, 63. https://pubs.usgs.gov/of/2011/1060/

Trugman, D. T., & Shearer, P. M. (2017). GrowClust: A hierarchical clustering algorithm for relative earthquake relocation, with application to the Spanish Springs and Sheldon, Nevada, earthquake sequences. *Seismological Research Letters*, *88*(2A), 379–391. https://doi.org/10.1785/0220160188

Vuan, A., Sugan, M., Chiaraluce, L., & Di Stefano, R. (2017). Improving the detection of low-magnitude seismicity preceding the Mw 6.3 L'Aquila earthquake: Development of a scalable code based on the cross-correlation of template earthquakes. *Bulletin of the Seismological Society of America*, *108* (1), 471–480. https://doi.org/10.1785/0120170106

Waldhauser, F., Michele, M., Chiaraluce, L., Di Stefano, R., & Schaff, D. P. (2021). Fault planes, fault zone structure and detachment fragmentation resolved with high-precision aftershock locations of the 2016–2017 Central Italy sequence. *Geophysical Research Letters*, *48*(16), e2021GL092918. https://doi.org/10.1029/2021GL092918

Walters, R. J., Gregory, L. C., Wedmore, L. N. J., Craig, T. J., McCaffrey, K., Wilkinson, M., et al. (2018). Dual control of fault intersections on stop-start rupture in the 2016 Central Italy seismic sequence. *Earth and Planetary Science Letters*, *500*, 1–14. https://doi.org/10.1016/j.epsl.2018.07.043

Wei, S., Helmberger, D., Owen, S., Graves, R. W., Hudnut, K. W., & Fielding, E. J. (2013). Complementary slip distributions of the largest earthquakes in the 2012 Brawley swarm, Imperial Valley, California. *Geophysical Research Letters*, *40*, 847–852. https://doi.org/10.1002/grl.50259

Wessel, P., Luis, J. F., Uieda, L., Scharroo, R., Wobbe, F., Smith, W. H. F., & Tian, D. (2019). The Generic Mapping tools version 6. *Geochemistry, Geophysics, Geosystems*, *20*, 5556–5564. https://doi.org/10.1029/2019GC008515

Yu, C., Li, Z., & Penna, T. (2018a). Interferometric synthetic aperture radar atmospheric correction using a GPS-based iterative tropospheric decomposition model. *Remote Sensing of Environment*, *204*, 109–121. https://doi.org/10.1016/j.rse.2017.10.038

Yu, C., Li, Z., Penna, N. T., & Crippa, P. (2018b). Generic atmospheric correction model for Interferometric Synthetic Aperture Radar observations. *Journal of Geophysical Research: Solid Earth*, *123*(10), 9202–9222. https://doi.org/10.1029/2017JB015305

Yu, C., Penna, N. T., & Li, Z. (2017). Generation of real-time mode high-resolution water vapor fields from GPS observations. *Journal of Geophysical Research: Atmospheres*, *122*, 2008–2025. https://doi.org/10.1002/2016JD025753

Zahradník, J., Gallovič, F., Sokos, E., Serpetsidaki, A., & Tselentis, G.-A. (2008). Quick fault-plane identification by a geometrical method: Application to the Mw6.2 Leonidio earthquake, January 6, 2008, Greece. *Seismological Research Letters*, *79*(5), 653–662. https://doi.org/10.1785/gssrl.79.5.653

Zahradník, J., & Sokos, E. (2014). The Mw 7.1 van, Eastern Turkey, earthquake 2011: Two-point source modelling by iterative deconvolution and non-negative least squares. *Geophysical Journal International*, *196*, 522–538. https://doi.org/10.1093/gji/ggt386

Zahradník, J., & Sokos, E. (2018). ISOLA Code for Multiple-Point Source Modeling—Review. In S. D'Amico (Ed.), *Moment Tensor Solutions* (pp. 1–28). Springer Natural Hazards. Springer. https://doi.org/10.1007/978-3-319-77359-9_1

Zhang, M., Ellsworth, W. L., & Beroza, G. C. (2019). Rapid earthquake association and location. *Seismological Research Letters*, *90*(6), 2276–2284. https://doi.org/10.1785/0220190052

Zhu, W., & Beroza, G. C. (2019). PhaseNet: A deep-neural-network-based seismic arrival-time picking method. *Geophysical Journal International*, *216*(1), 261–273. https://doi.org/10.1093/gji/ggy423